

Integrated Computational Aeroacoustics for UAM Design. Part 2. Noise Characterization Metrics

Daniel S. Little,* Doseph Majdalani, Daniel S. Little,* Daniel S. Little,*

This work identifies seven aeroacoustic post-processing metrics that facilitate urban air mobility (UAM) vehicle noise prediction. An increase in production and use of UAM and distributed electric propulsion (DEP) vehicles within populated civilian areas stands behind the need to minimize the noise produced by these vehicles. The FAA's strict noise regulations on UAM aircraft compels designers to place a significant emphasis, early in the design phase, on the characterization and analysis of the external noise produced by these vehicles, namely, to ensure their design viability. Whereas a number of codes such as ANOPP, WOPWOP, ASSPIN, CHARM, and so on, have been developed specifically for this purpose, they generally lack a friendly graphical user interface or an acoustics post-processing toolbox that can provide all of the metrics needed to secure the requisite aircraft certifications or required modifications. To overcome this deficiency, this work focuses on the analysis and interpretation of predicted noise signals using a set of characteristic metrics that can be instrumental in guiding the design process. Following a thorough review of metrics standardized by the International Civil Aviation Organization (ICAO) as well as the Federal Aviation Association (FAA), seven metrics are identified, evaluated, and discussed in the context of UAM noise prediction. When used in conjunction with FlightStream[®], a modern surface-vorticity panel code, these metrics are shown to provide a complementary assortment of tools to concisely describe UAM-based acoustic signal properties.

Nomenclature

 a_k, b_k real and imaginary parts of the Fourier coefficient

c speed of sound

DEP Distributed Electric Propulsion
EPNL Effective Perceived Noise Level
EPNdB Effective Perceived Noise Decibels
eVTOL Electric Vertical Take-Off and Landing

FFT Fast Fourier Transform
FAA Federal Aviation Association

f frequency, 1/T

 $f^{(c)}$ center frequency in a specific band f_i , K_i ith frequency or K coefficient

 $f^{(l)}$, $f^{(u)}$ lower and upper edge of frequency band ICAO International Civil Aviation Organization

N noisiness in units of noy OASPL Overall Sound Pressure Level

OASPL_A A-weighting Overall Sound Pressure Level PBS Proportional frequency-Band Spectrum

PNL Perceived Noise Level PNLdB Perceived Noise Decibels P_n nth pressure data point

PSD Power Spectral Density spectrum

 $p_{\rm ref}$ reference pressure

1

^{*}Graduate Research Assistant, Department of Aerospace Engineering. Member AIAA.

[†]Professor and Francis Chair, Department of Aerospace Engineering. Assoc. Fellow AIAA.

^{*}Walter and Virginia Woltosz Professor, Department of Aerospace Engineering; co-founder, Research in Flight. Assoc. Fellow AIAA.

[§]CEO, Research in Flight. Senior Member AIAA.

RVLT Revolutionary Vertical Lift Technology SEL, SPL Sound Exposure and Sound Pressure Levels

T signal period t_f, t_i final or initial time UAM Urban Air Mobility

 W_A, W_C A- and C-weighting functions

Greek Symbols

 α propeller's vertical pitch angle

 ϕ frequency phase γ ratio of specific heats

 Δf frequency bin or band width

Subscripts, Superscripts, and Indices

c, l, u central, lower, or higher frequencyk Discrete Fourier Transform (DFF) index

m band index

I. Introduction

A SUBSTANTIAL challenge posed to UAM vehicle design teams stands in collecting measured or predicted aeroacoustic signals and then reliably determining their favorable and adverse characteristics. Research in acoustics and sound may be traced as far back as 500 B.C., particularly, to Pythagorus and his discovery of a correlation between the length of a string and the pitch or frequency that it produces. He finds, for example, that by doubling the length of a string, the pitch is reduced by one octave relative to its original value [1]. One hundred and fifty years later, the Greek architect Polykleitos participates in the design of the Theater of Epidaurus, one of the most well-preserved assembly sites in ancient Greece. Roman architect and engineer Vitruvius later notes that this aesthetic structure is constructed in such a way to ensure that the acoustics are evenly distributed and distinct up to the uppermost seats, and that the voice meets "no obstruction." During that era, it is also noted how bronze sounding walls and vessels can be used to reinforce the tones generated by humans [2]. In the 6th century A.D., Roman philosopher Boethius publishes his work on the relation linking music, science, and human perception of sound; in it, he particularly calls attention to the frequency's bearing on the sound perceived by humans [3].

Skipping forward to the early part of the 16th century, French mathematician Mersenne, who is often referred to as the "father of acoustics," manages to develop preliminary statements describing the frequency of an audible tone and the frequency ratio between a note and its octave [4]. Further in the 16th and 17th centuries, the work of Hooke and Savart is known for ushering the development of what is now known as the Savart wheel, specifically, the first device capable of producing sound at a prescribed frequency [5]. In roughly the same period, attempts are made to experimentally measure the speed of sound in air. However, disparate results are obtained.

In the mid-sixteen hundreds, Gassendi attempts to calculate sound propagation using firearms and emerges with a value of approximately 478 m/s. Although he arrives at an imprecise value, he notes that the speed of sound does not depend on the pitch itself, contrary to a statement made by Aristotle a millennium earlier. Following Gassendi's experiment, Mersenne reports a slightly rectified value of 450 m/s [6]. This is followed by Borelli and Viviani, who jointly improve this measurement to 350 m/s. Around the same period, Bianconi independently deduces that the speed of sound must increase with temperature [7]. Meanwhile, a similar attempt at predicting the speed of sound through air is made by Newton. By assuming that air particles undergo a simple harmonic motion, Newton predicts a speed of sound equaling the square root of pressure over density, thus leading to slightly lower values than expected. His expression is soon adjusted by Laplace who, assuming adiabatic gas compression, determines that $c = (\gamma p/\rho)^{1/2}$ for the speed of sound [8].

In hindsight, the development of calculus by Newton and Leibniz during this epoch may be viewed as being invaluable at providing the necessary tools to formulate, derive, and solve the first wave equation. The required effort is actually carried out by D'Alembert in the mid-seventeen forties, the dawn of theoretical aeroacoustics [9]. Both Lagrange and Euler then independently extend the newly conceived calculus relations to pave the way for modern

acoustics. As such, and in the wake of Lagrange, Euler, and Newton, research in acoustics continues to flourish into the 19th century, particularly, through the efforts of von Helmholtz, Rayleigh, Stokes, and Kirchhoff, to name only a few.

For instance, around the mid-eighteen hundreds, German physiologist and physicist von Helmholtz manages to achieve a deeper understanding of the physiology of the human ear [10]. By observing the manner by which resonators in the cochlea are affected by alternating frequencies and tones, von Helmholtz points out how the quality of a tone results in unique resonator responses in the human ear [1]. This is followed by the construction of the Fast Fourier Transform (FFT), an efficient formulation of the Discrete Fourier Transform (DFT) by Gauss [11], which is popularized by Cooley and Tukey in 1965 [12]. Then in 1877, Lord Rayleigh publishes his *Theory of Sound* in two impressive volumes, with the second part being devoted to the theory of sound propagation in fluids [13]. While this work is being brought to fruition, Stokes continues to advance his theory on hydrodynamics, including his seminal contributions to the development of the Navier–Stokes equations in 1880 [14]. Along similar lines, Kirchoff, a German physicist with groundbreaking formulations in circuitry, spectroscopy, and blackbody radiation, makes substantial contributions in linear acoustics and mathematical physics. Among his many notable achievements, one may point out the Kirchhoff–Helmholtz integral and the Kirchhoff–Fresnel approximations for the analysis of single-edge diffraction and directional sound propagation.

Moving on to the nineteen fifties, and prompted in part by the need to mitigate jet engine noise, Lighthill pioneers several predictive formulations in aeroacoustics [15, 16]. His concepts quickly gain popularity and are later viewed as being quite foundational to the advancement of theoretical and computational acoustic analysis. Shortly thereafter, Lighthill's work is extended by Curle [17], Ffowcs Williams [18], and Lowson [19], eventually leading to the groundbreaking 1969 article by Ffowcs Williams and Hawkings [20]; the latter describes the acoustic contributions of sound emanating from a solid surface of arbitrary shape and propagating in a general direction through a fluid medium [20]; the resulting formulation is universally referred to as the Ffowcs Williams—Hawkings (FWH) equation. Four decades later, Farassat [21] obtains a closed-form solution to the FWH equation, which is quickly superseded by several reformulations [22–24], namely, the so-called "Formulation 1, Formulation 1A," and "Formulation 3." Due to their effectiveness and versatility, the last two formulations stand at the basis of several present-day subsonic and supersonic acoustics simulation packages, being embodied into ASSPIN/ASSPIN2, ANOPP/ANOPP2, PSU-WOPWOP, and others under production [25–27].

With the growing number of airports and aircraft operating amid civilian populations, the need to predict, control and suppress aircraft noise continues to receive attention in the acoustics research community. Examples include recent studies by McKay and Kingan [28], Jia and Lee [29], Lee and Lee [30], Gwak et al. [31], Smith et al. [32], Krishnamurthy et al. [33], Jeong et al. [34], Dbouk and Drikakis [35], Fenyvesi et al. [36], Ko et al. [37], and Yucel et al. [38]. With similar objectives in mind, the present work seeks to address the two-pronged nature of this problem. Not only must an aircraft designer identify the physical characteristics of a given signal, but also account for its human-perceived impact. In fact, the former issue is covered extensively in the fields of linear acoustics and signal analysis, particularly, through signal decomposition tools such as the Fast Fourier Transform (FFT) algorithm. Such a technique adequately resolves the frequency spectrum of a signal, while its pressure magnitude is further simplified using suitable measurements in terms of the decibel (dB) unit. The latter enables us to precisely assign values to physical noise intensities on a logarithmic scale that is congruent with the human auditory range, as envisioned by Bell and widely adopted since the 1931 edition of the NBS Standards Yearbook [39].

In complementing advances in acoustic measurement technology, the need to properly model the physiologically-perceived noise is addressed through the works of several scientists; these include von Bekesy, Rhode, Robles, Fletcher, and Munson. On the one hand, von Bekesy's nonlinear model of the inner ear earns him a 1962 Nobel prize in physiology [40]. Moreover, his framework proves instrumental to the experimental investigations of Rhode and Robles [41], whose measurements help to elucidate the nonlinearities affecting the growth response of particular signal frequencies and intensities. On the other hand, von Bekesy's results serve a vital role in corroborating the pioneering work of Fletcher and Munson [42], whose 1933 identification of "equal-loudness contours" for the human ear (see Fig. 1) remains one of the most cited works on the subject. Accordingly, the loudness curves are prescribed not necessarily by the signal frequency but, rather, by the signal intensity at a given frequency, as perceived by listeners. As such, each curve in Fig. 1 constitutes a line of "equal-loudness," in units of phons, as a function of both frequency and intensity. To some degree, the ensuing graphs provide a visual depiction of the formidable nonlinearities inherent to the auditory system. In fact, the development of Fletcher and Munson's curves would later incentivize the development of several useful metrics by which objective qualities of human-perceived signals produced by aircraft and industrial machinery could be quantified.

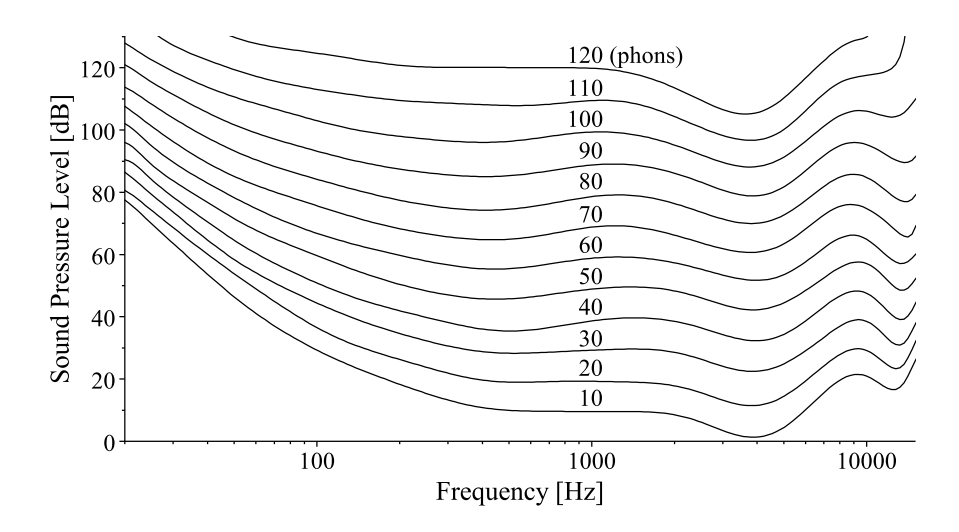


Fig. 1. Fletcher-Munson equal-loudness curves [42].

In this vein, and following the experimental work conducted by Fletcher and Munson [42], other studies that are inspired by technological developments have provided the basis for establishing additional aeroacoustic metrics. These have gradually gained popularity and used in aircraft regulatory policies, mainly, those that are developed and implemented by both the Federal Aviation Association (FAA) and the International Civil Aviation Organization (ICAO). The new metrics include, for example, the *Power Spectral Density* (PSD) spectrum (including the A-Weighting correction for a given signal), the *Proportional Band Spectrum* (PBS), the *Overall Sound Pressure Level* (OASPL), the *Sound Exposure Level* (SEL), the *Perceived Noise Level* (PNL), the *Tone-corrected Perceived Noise Level* (PNL-T), and the *Effective Perceived Noise Level* (EPNL). Such metrics serve to quantify the physical properties of a signal as well as account for the shift in intensity or perceived "annoyance" caused by noise due to the physiological sensitivity of an individual's auditory system.

In what follows, the coupling of these two approaches, i.e., the physical description of a particular signal as well as its human-perceived characterization, will be jointly used to provide a framework to evaluate a set of seven metrics that are capable of providing an effective description of the external noise generated by a specific vehicle design.

II. Metrics: Specific Formulations and Significance

A. Identifying Metrics of Broad Interest

The multi-faceted field of aeroacoustics extends into almost every type of fluid flow application, with an equivalent number of metrics describing each problem. Because of the subject's broadness, the identification of essential metrics requires concentration on a select few metrics that are capable of providing a complete but concise characterization of an externally observed signal. To be specific, the metrics must describe both physical and perceived properties at an observer's location. Recognizing that the latter is a function of the former, we turn our attention first to metrics that describe a signal's physical constitution.

With the end goal of designing an aircraft that can successfully meet acoustic regulations, we begin by performing a review of metrics standardized by the ICAO and FAA. Through this search, a total of seven metrics are identified as measurements of interest; four of those describe a signal's physical makeup, and two metrics attempt to evaluate the human-perceived signal. These metrics, when viewed collectively, produce a clear and concise description of the aeroacoustic signal structure. As such, in describing the physical makeup of a signal, both the frequency-domain and time-domain components are quantified using the PSD spectrum, the PBS, the OASPL, and the SEL. In an effort to describe the human perceived characteristics, three additional metrics are selected. These consist of the PNL, the PNL-T, and the EPNL. In what follows, these seven metrics are described in slightly more detail.

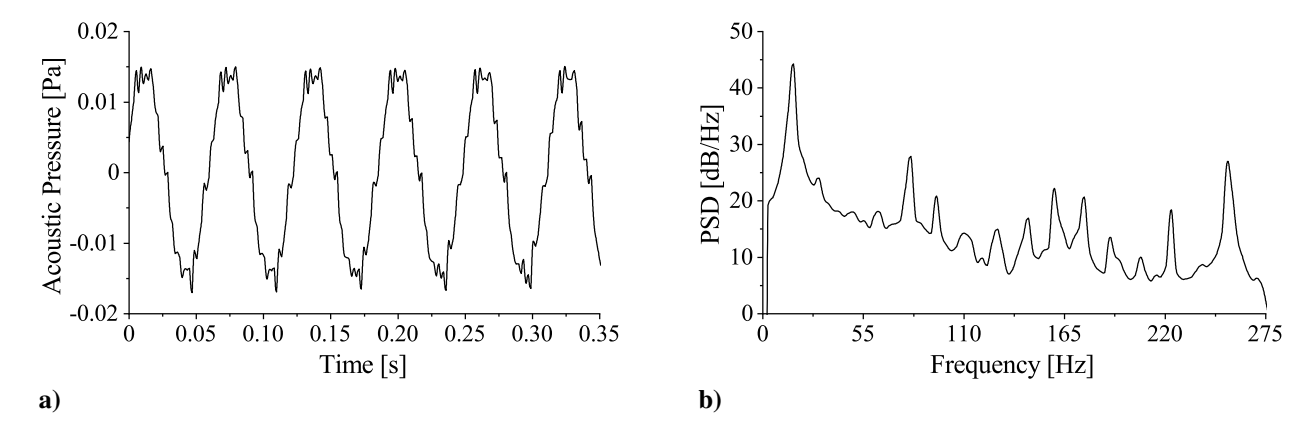


Fig. 2. Illustration of a) the pressure-time history and b) Power Spectral Density (PSD) spectrum of a representative UAM flyover.

B. Power Spectral Density Spectrum (PSD)

The PSD quantifies the physical variance of pressure as a function of frequency in units of Pa²/Hz. It describes the distribution of power into the frequency bins or bands that form the signal. For propeller-driven vehicles, peaks arise along frequencies pertaining to primary propeller angular speeds, and these are typically accompanied by diminishing peaks at blade harmonic frequencies. In the interest of clarity, the PSD of a UAM vehicle flyover is visualized in Fig. 2b side-by-side with the pressure's time history, which is provided in Fig. 2a. Therein, a principal peak can be seen at roughly 150 Hz, with several diminishing peaks above and below this frequency. For propeller-driven vehicles with multiple blade sizes, the PSD is capable of revealing the frequency at which the largest amount of power is being expended. The PSD calculation often serves as the first step in signal analysis because of its ability to provide an accurate accounting of the physical "ingredients" or frequencies that constitute a signal.

The PSD is calculated by first Fourier transforming a pressure-time signal into its complex Fourier coefficients; the latter enable us to then extract the pressure wave amplitude and corresponding phase angle at any given frequency. As for the discrete Fourier transform (DFT), it converts a sequence of N pressure amplitudes as a function of time, $p_n = \{p_0, p_1, p_2, \dots, p_{N-1}\}$ into another sequence of N complex valued pressure data points, $P_k = \{P_0, P_1, P_2, \dots, P_{N-1}\}$. The discrete Fourier transform is subsequently processed by evaluating:

$$P_{k} = \sum_{n=0}^{N-1} p_{n} e^{-\frac{i2\pi}{N}kn} = \sum_{n=0}^{N-1} p_{n} \left[\cos \left(\frac{2\pi}{N} kn \right) - i \sin \left(\frac{2\pi}{N} kn \right) \right]; \quad k = \{0, 1, 2, \dots, N-1\}.$$
 (1)

1. DFT and FFT

In practice, the DFT can be characterized by a unique matrix that encapsulates the overall transformation. However, because of the computational expense of this technique, the Fast Fourier Transform (FFT) algorithm is often substituted to reduce the ensuing effort, namely, by taking advantage of the symmetry underlying the DFT matrix. Credit for the FFT's modern formulation and popularization is often given to James Cooley and John Tukey, whose work in 1965 has become recognized among the most significant and widest-reaching breakthroughs in computational science [12]. For the reader's convenience, more detail on the DFT matrix manipulation, which is followed by the FFT algorithm and its implementation in the context of this study, are provided in Appendices A and B, respectively. As shown therein, the PSD can be resolved by scaling the resultant sequence P_k using

$$PSD(f_k) = \begin{cases} \frac{|P_k|^2}{N^2} T; & k = 0, \\ 2\frac{|P_k|^2}{N^2} T; & 1 \le k \le \frac{1}{2}N - 1, \\ \frac{|P_k|^2}{N^2} T; & k = \frac{1}{2}N. \end{cases}$$
 (2)

In the above, $|P_k|^2 = a_k^2 + b_k^2$, whereas a_k and b_k stand for the real and imaginary parts of the Fourier coefficients, respectively. As for ϕ_k , which represents the phase at a given frequency k, it may be readily determined from

$$\phi_k = \tan^{-1} \left(\frac{b_k}{a_k} \right). \tag{3}$$

Note that the bin-width in the PSD scheme is simply

$$\Delta f = \frac{1}{T},\tag{4}$$

where T denotes the period of the signal. It may be noted that only coefficients up to N/2 are used in the PSD calculation. Since the Fourier transform for real signals, such as pressure-time signals, is mirrored on the left and right-hand sides of the (N/2)th point, only N/2 data points are required in the PSD computation.

C. A-Weighting (W_A)

While the PSD results lead to deeper insight into the physical makeup of the signal, it does not account for the human perception of the sound. Because the human-perceived intensity of a signal depends heavily on the intensity of the signal as well as its frequency, this effect is accounted for using a weighting function. At the time of this writing, weighting functions are standardized by the International Electrotechnical Commission (IEC), and the most suitable function to adequately adjust for human sound perception is referred to as *A-weighting*. Its incorporation into PSD calculations can be undertaken rather straightforwardly by calculating:

$$W_A(f) = \frac{K_3 f^4 W_c}{\left(f^2 + f_2^2\right) \left(f^2 + f_3^2\right)}; \qquad W_C(f) = \frac{K_1 f^4}{\left(f^2 + f_1^2\right)^2 \left(f^2 + f_4^2\right)^2},\tag{5}$$

where

$$K_1 = 2.242881 \times 10^{16}$$
, $K_3 = 1.562339$, $f_1 = 20.598997$, $f_2 = 107.65265$, $f_3 = 737.86233$, and $f_4 = 12194.217$. (6)

In the process of accounting for physiological perceptions, the A-weighting serves to gradually attenuate pressure amplitudes at frequencies that fall above and below 1000 Hz, i.e., the frequency at which the human ear tends to be most sensitive. By way of illustration, Fig. 3a is used to depict the unweighted PSD for the UAM flyover case under consideration, whose A-weighted counterpart is presented in Fig. 3b. Clearly, the A-weighting rectifies the PSD distribution quite appreciably, namely, in a manner that is commensurate with its perceived impact on human hearing.

D. Proportional Band Spectrum (PBS)

When analyzing broadband noise, such as jet engine mixing and turbulence, as opposed to signals comprised of several discrete signals (e.g., those generated by propeller-driven aircraft), the PSD does not produce well-defined

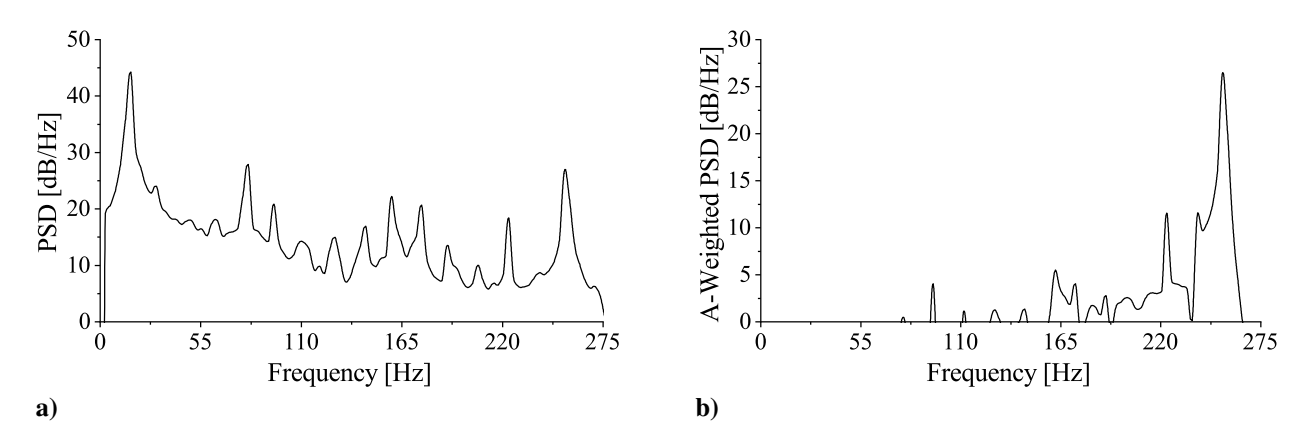


Fig. 3. Side-by-side comparison of a) unweighted and b) A-weighted Power Spectral Density (PSD) spectra originating from the same signal.

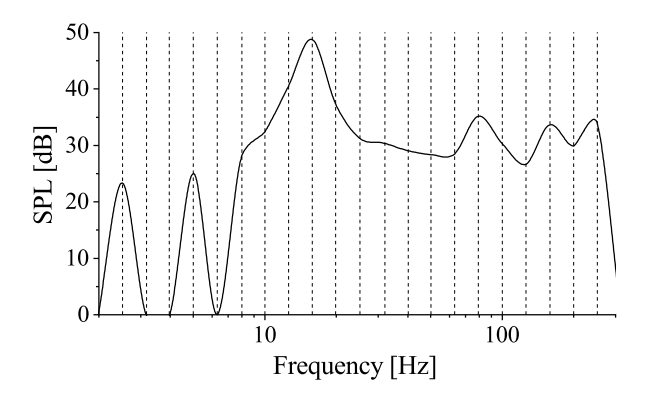


Fig. 4. Proportional (frequency) Band Spectrum (PBS) of the unweighted signal of Fig. 3a showing the SPL within 1/3-octave frequency bands on a log₁₀-based scale.

peaks such as those observed in the present data set. For such cases, it is useful to evaluate the integrated pressure or Sound Pressure Level (SPL) over larger bands of frequency. This metric, which is referred to as the *Proportional Band Spectrum* (PBS), is illustrated in Fig. 4.

In practice, the PBS is commonly used to analyze noise distributed over a wide frequency range. It is comprised of 40 frequency bins, each spanning 1/3-octave. The bins have a frequency range of 1 – 10,000 Hz, where the 30th band extends around a central frequency of 1000 Hz. Using the unweighted PSD in Fig. 3a as an example, its corresponding PBS in Fig. 4 displays the individual contributions of each 1/3-octave frequency band to the total signal SPL.

Interestingly, an octave band is defined as one where the upper edge of the band is twice the frequency of its lower edge, specifically, $f^{(u)} = 2f^{(l)}$, where the superscripts refer to "upper" and "lower." The relation between upper and lower edges of $1/N_0$ -octave frequency bands can be written as $f^{(u)} = 2^{1/N_0} f^{(l)}$. In this context, the edge ratio for 1/3-octave bands may be determined from $f^{(u)} = 2^{1/3} f^{(l)}$. As for the band central frequency, it is given by $f^{(c)} = 2^{1/6} f^{(l)}$ or $f^{(c)} = 2^{-1/6} f^{(u)}$, where the superscript "c" stands for "center."

In Fig. 4, vertical lines are drawn to depict the centers of the proportional frequency bands. The American National Standards Institute (ANSI) defines the PBS bands using a base-10 rather than a base-2 formulation, as shown above [39]. The relation between upper and lower bands on a base-10 scale is then given by

$$f^{(u)} = 10^{0.3} f^{(l)}. (7)$$

In this context, the band central frequencies may be deduced from

$$f^{(c)} = 10^{0.6} f^{(l)}$$
 or $f^{(c)} = 10^{-0.6} f^{(u)}$. (8)

It should be noted that the value assigned to a given frequency bin, m, can be obtained by integrating the unweighted PSD over the frequency range of each bin. One gets:

$$\left\langle p^{2}\right\rangle _{m}=\int_{f_{m}^{(l)}}^{f_{m}^{(u)}}\mathrm{PSD}\left(f\right) \mathrm{d}f. \tag{9}$$

Similarly, for a discrete PSD, this integral becomes

$$\langle p^2 \rangle_m = \sum_{i=1}^{N_m} \text{PSD}(f) \, \Delta f,$$
 (10)

where $\langle p^2 \rangle_m$, N_m , and Δf denote the squared mean pressure, number of PSD points, and PSD frequency resolution within each bin m, respectively. For convenience, it is customary to present the PBS on a logarithmic scale using units of dB rather than Pa², as shown presently. The conversion from Pa² to dB follows from

$$SPL_m = 10\log_{10}\left(\frac{\left\langle p^2\right\rangle_m}{p_{\text{ref}}^2}\right),\tag{11}$$

where p_{ref} represents the standard reference pressure, i.e., 2×10^{-5} Pa.



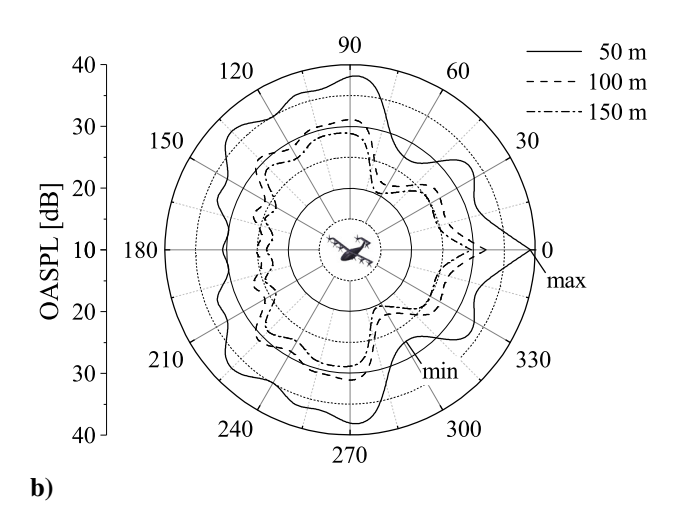


Fig. 5. Sketch of a) representative vehicle based on the OpenVSP NASA Revolutionary Vertical Lift Technology (RVLT) Tiltwing UAM eVTOL concept and b) its OASPL recorded at 36 equispaced observers located at 50 m, 100 m, and 150 m away from the vehicle's centroid.

E. Overall Sound Pressure Level (OASPL)

The Overall Sound Pressure Level (OASPL) is commonly used to quantify the overall loudness of a signal at some observer location. To recall, loudness is the perceived intensity of the sound and the OASPL returns a single value for the loudness of some event, such as an aircraft flyover. This figure of merit may be calculated from either a weighted or unweighted Proportional Band Spectrum. Its calculation follows the same idea behind the proportional band analysis, except for using an infinite bandwidth. This can be accomplished by taking,

$$\langle p^2 \rangle_{\text{OASPL}} = \sum_{m=1}^{M} \text{PSD}(f)_m \Delta f,$$
 (12)

where M denotes the total number of bins contributing to the PSD. In decibel units, the OASPL can be calculated from

$$SPL_{overall} = 10log_{10} \left(\frac{\langle p^2 \rangle_{OASPL}}{p_{ref}^2} \right).$$
 (13)

The OASPL commonly serves two objectives: the first being the visualization of a power distribution in a field of observers, and the second being an OASPL-time history for Sound Exposure Level (SEL) computation, which is an essential metric for small aircraft certification. The generation of such plots requires the use of multiple observers that are distributed in a logical manner within the field of interest. In this fashion, a visual representation of the bulk direction of the signal power can be realized around the source.

In the interest of clarity, a representative vehicle is chosen based on an open-source model configuration that is supplied publicly as an Open Vehicle Sketch Pad (OpenVSP) geometric file of a UAM concept from NASA's library. As shown in Fig. 5a, this particular Revolutionary Vertical Lift Technology (RVLT) vehicle carries eight 5-bladed propellers operating at 1420 RPM and a tip Mach number of 0.5. The vehicle is simulated in forward-flight mode at a zero degree angle of incidence and a cruise speed of 20 m/s. Using the metric described above, its OASPL map is readily generated and showcased in Fig. 5b. The corresponding graph depicts three particular lines of constant OASPL taken at observer distances of 50 m, 100 m, and 150 m from the aircraft's centroid. Based on these contours, one may directly infer that, at the 50 m distance from the vehicle, the peak OASPL value of 38 db occurs at $\theta = 0^{\circ}$ and that the minimum OASPL of 28 dB appears at both 55° and 305°, symmetrically about the vehicle's axis. These values shift to 22 dB and 20 dB as the distance from the vehicle is increased to 150 m. These OASPL maps prove very useful at characterizing the sound field around a vehicle, as it will be further demonstrated using three detailed UAM configurations in Sec. III below.

F. Sound Exposure Level (SEL)

The Sound Exposure Level (SEL) is the first of the two metrics used in ICAO and FAA certifications, with the other being the Effective Perceived Noise Level (EPNL). The SEL is primarily used for small aircraft and follows directly from the time-history of an A-weighted OASPL. The SEL characterizes the perceived intensity or loudness from a single noise event. It returns a constant sound pressure level that carries the same amount of energy in one second as the original noise event. It is employed in the certification of propeller-driven light airplanes and light helicopters. To compute the SEL, one evaluates the following expression:

$$SEL = 10\log_{10}\left(\frac{1}{T}\int_{t_i}^{t_f} 10^{OASPL_A/10} dt\right),$$
(14)

where T = 1s represents a normalizing time constant whereas t_i and t_f denote the initial and final time steps of the original signal, respectively. The time-dependent OASPL metric can be derived from a pressure-time signal discretized into 0.5 s intervals, for which a single OASPL value is calculated at each interval. For the case of an observer that is moving with the vehicle, the SEL expression simplifies into

$$SEL = OASPL_A + 10log_{10} \left(t_f - t_i \right). \tag{15}$$

G. Perceived Noise Level (PNL) and Tone-Corrected Perceived Noise Level (PNL-T)

To measure the *noisiness* (objective annoyance) of an event, the *Perceived Noise Level* (PNL) is commonly employed. The PNL is measured in perceived noise decibels. Numerically, the PNL is equal to a random noise-band of width 1/3-octave, whose center frequency is 1000 Hz, and which is considered by listeners to be *equally noisy*. Often, the original signal is discretized into multiple time segments, where a PNL is calculated for each segment. This, in turn, provides a PNL-time history of the signal. This particular procedure is then repeated for the evaluation of the *Effective Perceived Noise Level* (EPNL), whose calculation requires a tone-corrected PNL time history. The *Tone-corrected PNL*, commonly referred to as PNL-T or PNLT, increases the noise level to account for the impact of discrete tones within the spectra, particularly, those that are deemed to be more annoying, on average, than broadband noise of the same magnitude. The determination of PNL and PNLT values are standardized by the ICAO and follow the strategy described below.

1. PNL/PNLT Calculation

The PNL calculation is started by first determining the *perceived noisiness*, N, in units of "noys" within PBS bands between 50 and 10 kHz:

$$N = \begin{cases} 10^{M(c)[SPL-SPL(c)]} & SPL \ge SPL(a), \\ 10^{M(b)[SPL-SPL(b)]} & SPL(b) \le SPL < SPL(a), \\ 0.3 \times 10^{M(e)[SPL-SPL(e)]} & SPL(e) \le SPL < SPL(b), \\ 0.1 \times 10^{M(d)[SPL-SPL(d)]} & SPL(d) \le SPL < SPL(e). \end{cases}$$
(16)

In the above, the corresponding coefficients are given by Fig. 6. Once the values of N are found for each 1/3-octave band, the *total perceived noisiness* can be determined from

$$N_{t} = 0.85N_{\text{max}} + 0.15 \sum_{i=1}^{24} N_{i},$$
(17)

where *i* is the band index. The PNL is then calculated using

$$PNL = 40 + \frac{10}{\log_{10} 2} \log_{10}(N_t).$$
 (18)

The PNLT follows from 10 standardized steps presented below.

Step 1: For frequency bands starting at 80 Hz, calculate the slopes between bands as follows:

$$s_3$$
 = no value,

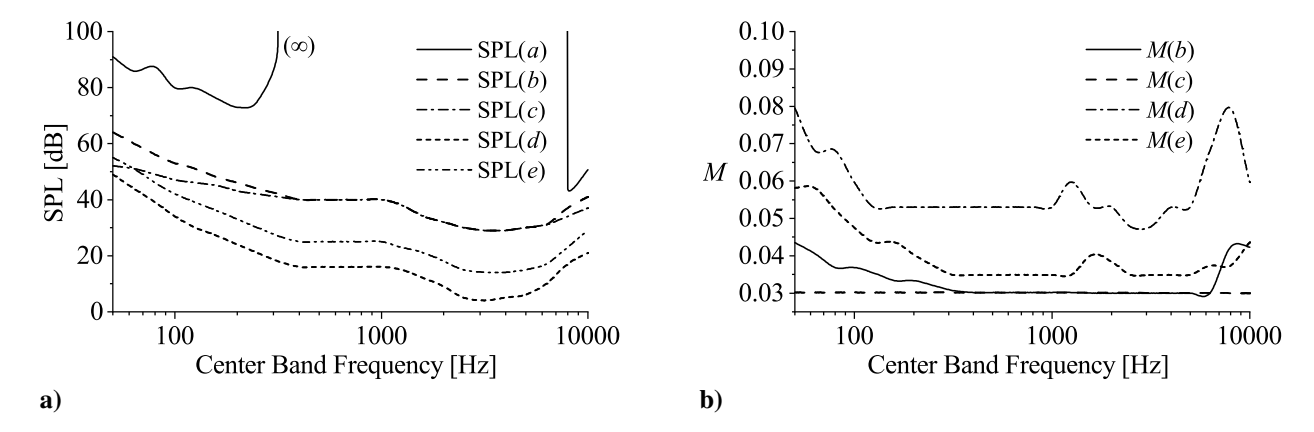


Fig. 6. Noy coefficients for a) SPL(a), SPL(b), SPL(c), SPL(d), and SPL(e) as well as b) M(b), M(c), M(d), and M(e).

$$s_4 = \text{SPL}_4 - \text{SPL}_3,$$

 $s_5 = \text{SPL}_4 - \text{SPL}_4,$
...
 $s_{24} = \text{SPL}_{24} - \text{SPL}_{23}.$

Step 2: Encircle the values of s_i , where the absolute value in the difference, $s_{i+1} - s_i$, is greater than five; that is, where

$$|\Delta s_i| = |s_{i+1} - s_i| > 5.$$

Step 3:

- 1. If the encircled value of the slope s_i is positive and algebraically greater than s_{i-1} , encircle SPL_i .
- 2. If the encircled value of slope s_i is less than or equal to zero, and s_{i-1} is positive, encircle SPL_{i-1} .

Step 4: Compute the adjusted sound pressure levels, SPL'_i.

- 1. For non-encircled SPLs, set $SPL'_i = SPL_i$.
- 2. For encircled SPLs in bands 1 through 23, perform the following:

$$SPL'_{i} = \frac{1}{2} \left(SPL_{i-1} + SPL_{i+1} \right).$$

3. If the sound pressure level in the highest band is encircled, let

$$SPL'_{24} = SPL'_{23} + s_{23}$$
.

Step 5: Compute new slopes s_i' , including an additional 25th band, by putting:

$$s'_{3} = s'_{4},$$
 $s'_{4} = SPL'_{4} - SPL'_{3},$
...
 $s'_{i} = SPL'_{i} - SPL'_{i-1},$
...
 $s'_{25} = s'_{24}.$
10

American Institute of Aeronautics and Astronautics

Step 6: For bands 3 through 23, compute the average slope between three adjacent slopes using:

$$\bar{s}_i = \frac{s_i + s_{i+1} + s_{i+2}}{3}.$$

Step 7: Compute one final adjusted sound pressure level, SPL''_i , beginning with i = 3 to 24, by taking:

$$SPL_{3}'' = SPL_{3},$$

$$SPL_{4}'' = SPL_{3} + \overline{s}_{3},$$

$$SPL_{5}'' = SPL_{4} + \overline{s}_{4},$$
...
$$SPL_{i}'' = SPL_{i-1} + \overline{s}_{i-1},$$
...
$$SPL_{24}'' = SPL_{23} + \overline{s}_{23}.$$

Step 8: Calculate the difference between the original SPL and the final adjusted SPL using:

$$F_i = SPL_i - SPL_i^{"}$$
.

Step 9: The frequency correction, C_i , can now be determined as follows: For frequency bands of $50 \le f_i < 500$,

$$C_{i} = \begin{cases} 0 & F < 1\frac{1}{2}, \\ \frac{1}{3}F - \frac{1}{2} & 1\frac{1}{2} \le F < 3, \\ \frac{1}{6}F & 3 \le F < 20, \\ 3\frac{1}{3} & 20 \le F. \end{cases}$$
(19)

For frequency bands of $500 \le f_i < 5000$,

$$C_{i} = \begin{cases} 0 & F < 1\frac{1}{2}, \\ \frac{2}{3}F - 1 & 1\frac{1}{2} \le F < 3, \\ \frac{1}{3}F & 3 \le F < 20, \\ 6\frac{2}{3} & 20 \le F. \end{cases}$$
 (20)

For frequency bands of $5000 \le f_i < 10000$,

$$C_{i} = \begin{cases} 0 & F < 1\frac{1}{2}, \\ \frac{1}{3}F - \frac{1}{2} & 1\frac{1}{2} \le F < 3, \\ \frac{1}{6}F & 3 \le F < 20, \\ 3\frac{1}{3} & 20 \le F. \end{cases}$$
(21)

 $\pmb{Step~10} \hbox{: The Tone-corrected Perceived Noise Level (PNL-T) can then be deduced from:}\\$

$$PNLT = PNL + C_{max}.$$
 (22)

H. Effective Perceived Noise Level (EPNL)

The Effective Perceived Noise Level (EPNL), which serves as the second ICAO certification metric, is primarily employed in the certification of large airplanes and heavy helicopters. The EPNL consists of a single value quantifying the relative noisiness (annoyance) of an individual aircraft fly-by event. According to the ICAO Annex 16:

"... EPNL shall consist of instantaneous perceived noise level, PNLT, corrected for spectral irregularities (the correction, called 'tone correction factor,' is made for the maximum tone only at each increment of time) and for duration."

"Three basic physical properties of sound pressure shall be measured: level, frequency distribution, and time variation. More specifically, the instantaneous sound pressure level in each of 24 one-third octave bands of the noise shall be required for each *one-half second* increment of time during the airplane flyover."

It can therefore be seen that the EPNL takes a given PNLT-time history, in one-half second increments, and integrates the portion of the signal that falls within 10 dB of the peak. Mathematically, this corresponds to the following integral:

EPNL =
$$10\log_{10}\left(\frac{1}{T}\int_{t_i}^{t_f} 10^{\frac{PNLT}{10}} dt\right),$$
 (23)

where T consists of a normalizing constant of 1 second. The integration limits t_i and t_f represent the times corresponding to the portion of the signal that falls within 10 dB of the peak PNLT measurement. It is important to note that all portions between t_i and t_f are included, regardless of whether the signal drops below 10 dB of the maximum measured value at any point between t_i and t_f . Similarly to the SEL, for a fixed observer in the vehicle's frame of reference, the PNLT term inside the integral is constant, and thus simplifies the resulting equation to the form

III. Demonstrative Cases

To illustrate how these metrics can be employed in a real-world application, several UAM type aircraft are analyzed using an acoustic module developed in-house for FlightStream[®], a modern, surface-vorticity flow solver. The advantages of utilizing surface-vorticity and vortex methods have been demonstrated in several related applications by Wu et al. [43], Ahuja et al. [44, 45], Ahuja and Hartfield [46], Faure and Leogrande [47], Faure et al. [48], and Fenyvesi et al. [36]. The solver itself has also undergone stringent validation studies by NASA researchers [49] as well as the UAM community [46, 50, 51]. To this end, numerical measurements (data) are extracted from the solver and further analyzed using several of the metrics previously defined. These metrics work together to fully characterize the impact of noise by providing a crisp landscape of the acoustic signatures produced around each representative vehicle.



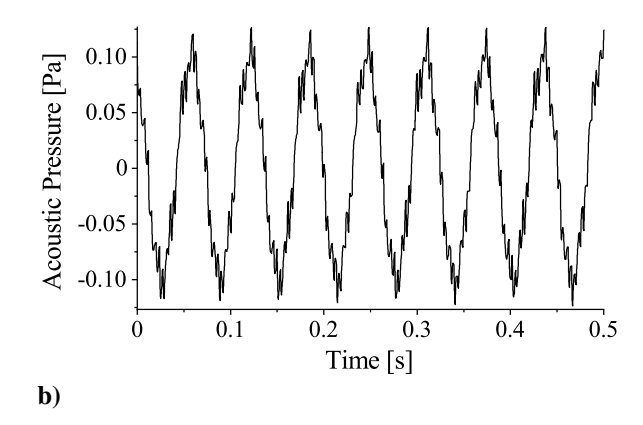


Fig. 7. Sketch of a) aircraft vehicle 1 based on the OpenVSP single-propeller Joby S4 UAM eVTOL concept and b) its pressure-time history recorded at the peak observer angle (290°) leading to the maximum in-plane OASPL (65.6 dB) at 50 m from the vehicle's active propeller.

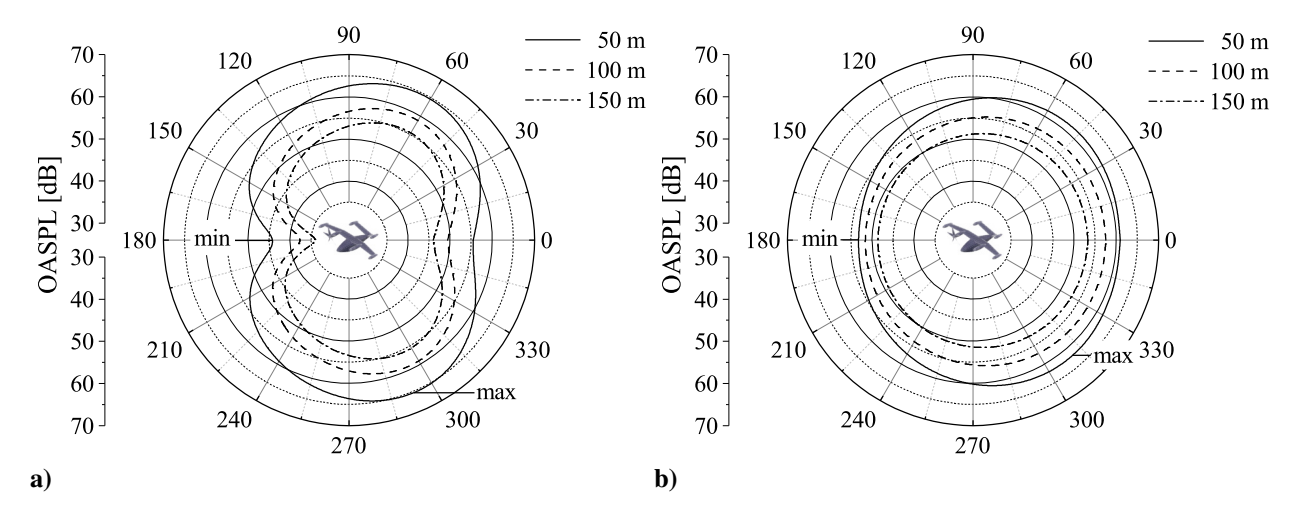


Fig. 8. Vehicle 1 OASPL vs. observer angle for a) three in-plane observers located at 50 m, 100 m, and 150 m horizontal radii around the vehicle's active propeller b) three out-of-plane observers located at a 50 m horizontal radius and situated at a vertical distance of 50 m, 100 m, and 150 m below the aircraft.

A. Case 1: Full UAM Vehicle with Isolated Propeller

The first example that we consider focuses on a single 5-bladed propeller on a contemporary UAM aircraft that is shown in Fig. 7a. The prototype chosen for this simulation corresponds to the publicly-available NASA OpenVSP model of the Joby S4 UAM eVTOL vehicle. The model is transferred from OpenVSP into FlightStream[®] as a Plot3D geometry with both solid and thin-surface representations of the propeller blades. More specifically, the fuselage, wings, and nacelles are Boolean-united in OpenVSP and then imported into FlightStream[®]. The propeller is operated at a speed of 955 RPM with a vertical pitch of $\alpha = 0^{\circ}$ and a tip Mach number of Ma = 0.4. As usual, the propeller's pitch represents the angle subtended between the rotor disc's horizontal plane of rotation and the blade's chord line.

The acoustic signal histories are generated at 36 microphones that are distributed in the form of a circular array with a radial range of 50 m within the plane of the aircraft and centered about the rotor hub. Each microphone is separated from its neighbor by an azimuthal angle of 10°, where pressure-time signals are recorded for each observer and then post-processed to retrieve the OASPL at each observer location. A sample pressure-time signal recorded at the angle of maximum in-plane OASPL (290°) is illustrated in Fig. 7b. The cumulative OASPL values of each observer are subsequently displayed on a polar chart in Fig. 8a. Therein, the locus of lowest and largest OASPL values are marked.

Along with the in-plane data, additional measurements are obtained in the out-of-plane field. This is accomplished by lowering the first observer circle with a 50 m fixed radius to vertical distances of 50 m, 100 m, and 150 m below the aircraft. The out-of-plane recorded measurements are then displayed in Fig. 8b. Although the general trends remain similar, moving below the aircraft reduces the sharp deviations in the curves that are caused by direct proximity to the propeller location. This may be attributed to the geometric smoothing of the distances from the source as the measurement plane is progressively shifted below the aircraft. Nonetheless, the locations of minimum and maximum OASPL remain virtually unchanged, although the angular distribution of the OASPL becomes gradually more uniform with successive increases in the vertical distance from the plane, a feature that could not be captured solely through in-plane measurements.

Based on the resulting visual representation, one may readily identify the points around the aircraft that are most sensitive to the sound projected by the propeller. Note that air flow is convected from the 180°–0° line into the propeller facing the 180° station. As expected, the loudest signals of approximately 65 dB are detected at essentially right angles to the propeller blades, looking at the tips of the blades. This is expected because the normal velocity of the blade (toward the observer) is the highest and thus produces the largest signal intensity at this location.

It should be noted that the total acoustic signal is comprised of both large and small sinusoidal waves of different frequencies. These correspond to the primary propeller frequency of 955 RPM, the five-bladed passage frequency, and their respective harmonics. The corresponding characteristics of the pressure time signal shown in Fig. 7b are reflected in the frequency domain analysis of this signal, which is provided using both unweighted and A-weighted PSD computations in Fig. 9a.

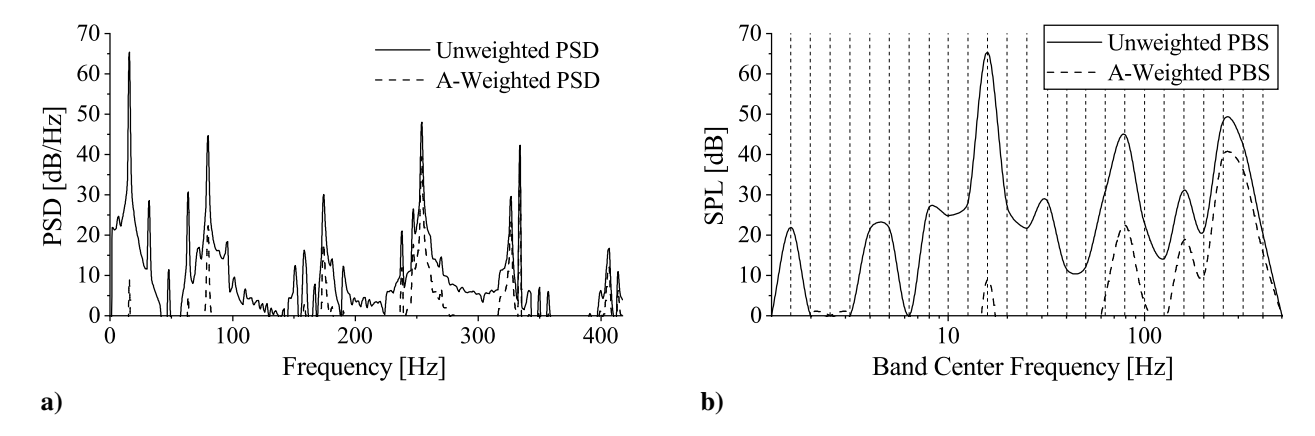


Fig. 9. Vehicle 1 distribution of both unweighted and A-weighted a) PSD and b) PBS measurements.

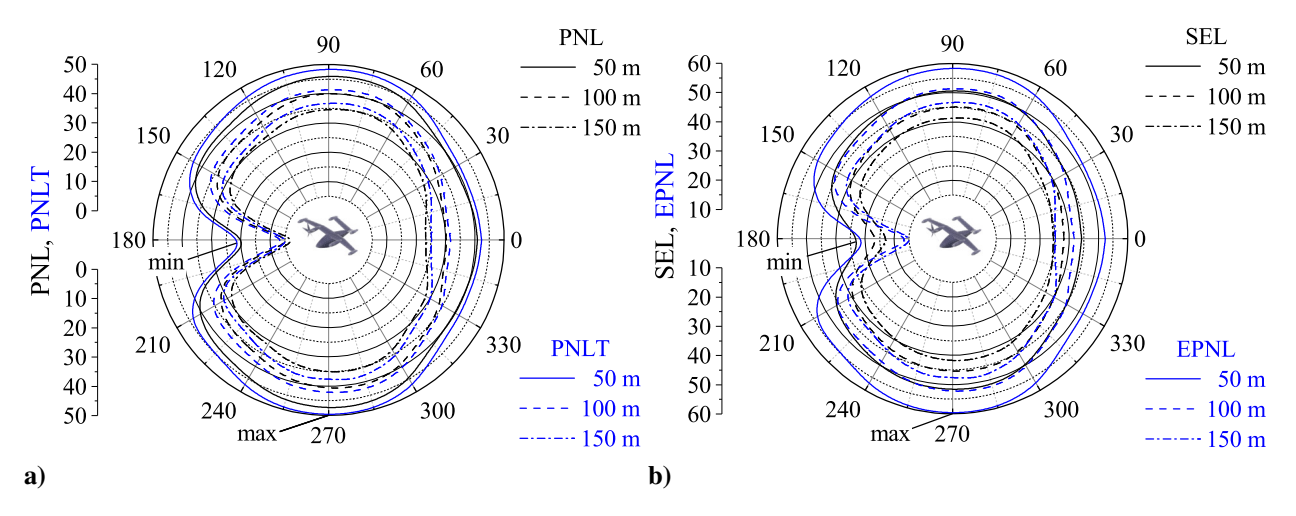


Fig. 10. Vehicle 1 distribution of a) PNL and PNLT as well as b) SEL and EPNL measurements acquired at three in-plane observers located at 50 m, 100 m, and 150 m from the vehicle's active propeller.

Based on this graph, it is apparent that the largest physical contribution stems from the propeller revolution rate (15.9 Hz), with the 5th (80 Hz), 10th (160 Hz), 15th (238 Hz), and 20th (320 Hz) harmonics being secondary contributors; nonetheless, the most significant *perceived* contribution to the overall noise appears to be near the 15th harmonic. In practice, this corresponds to a frequency spike in Fig. 9a near 238 Hz in both weighted and unweighted calculations. In the recorded data, the precise spike location appears at 254 Hz. This shift away from the expected harmonic tone is realized across all primary signal contributors except for the primary rotation rate of 15.9 Hz and its 5th harmonic of 79.6 Hz. The corresponding anomaly may be caused by constructive and destructive interference between signals radiating off different propeller blades. Note that a five-bladed propeller translates into a *blade passage frequency* that is five times higher than the overall propeller revolution rate. It is for this reason that the largest contributors to signal power appear in frequency multiples of 5 times the propeller revolution rate. Next, in complementing this analysis, Fig. 9b is used to display the 1/3-octave frequency bands, whose center frequency is denoted by vertical dashed lines. These range from approximately 1 Hz to 400 Hz and capture the frequency band's proportionate dB contribution to the OASPL. Graphically, one may infer that the largest physical (unweighted) and perceived (A-weighted) frequency band contributions stem from the 1/3-octave band centered at approximately 80 Hz.

In the interest of completeness, the remaining four characteristic metrics for vehicle 1, namely, the PNL, PNLT, SEL, and EPNL, are evaluated and shown in Fig. 10. Therein, the PNL and PNLT are paired side-by-side with the SEL and EPNL measurements at three different distances from the vehicle's rotor. Graphically, one can infer from Fig. 10a that the inclusion of a tone-correction leads to a higher perceived loudness level at all observer locations. This behavior could have been, perhaps, anticipated, because the presence of a pure tone in a signal creates the sensation of

a louder noise. In fact, tone-correction effects are particularly prominent in Fig. 10b where contours of SEL and EPNL measurements are furnished. Since only the EPNL incorporates a tone-correction, it is markedly larger at nearly all detection points. Moreover, it may be seen that the overall shapes of the contours in Fig. 10 tend to resemble those of the OASPL in Fig. 8, except for the more accentuated distortion of the lobe formation around the 180°–0° line. The increased sound directionality and resulting differences also lead to a distinct shift from 285°in the locus of peak values relative to the OASPL contours. More specifically, the maximum values and locations of the PNL, PNLT, SEL, and EPNL are found to be 47.6 PNLdB (270°), 49.9 PNLdB (270°), 51.9 dB (280°), and 59.9 dB (270°), respectively.

B. Case 2: Full UAM Vehicle with Multiple In-Phase Propellers

In the second case study, the remaining five propellers on the S4 UAM vehicle are enabled. Moreover, all propellers are operated synchronously at 955 RPM (15.9 Hz). In this case, the tip Mach number is kept at Ma = 0.4 and the vehicle is operated in forward-flight mode. Hover modes for this vehicle are also directly possible and additional case studies can be undertaken using the present framework. This UAM vehicle configuration is shown in Fig. 11a.

Once again, 36 stationary microphones are seeded in the form of a circular array at different radii with ranges of 50 m, 100 m, and 150 m, respectively; these microphones are placed in the plane defined by the forward velocity vector and an adjacent line running through the vehicle's centroid in level flight. As before, each microphone is separated from its neighbor by an azimuthal angle of 10°. For each observer, a pressure-time signal is recorded (see Fig. 11b) and then transformed into the frequency domain using both unweighted and A-weighted PSD spectra, as shown in Fig. 12a. Consistently with the single propeller case, we find in Fig. 12a that most of the signal power stems from

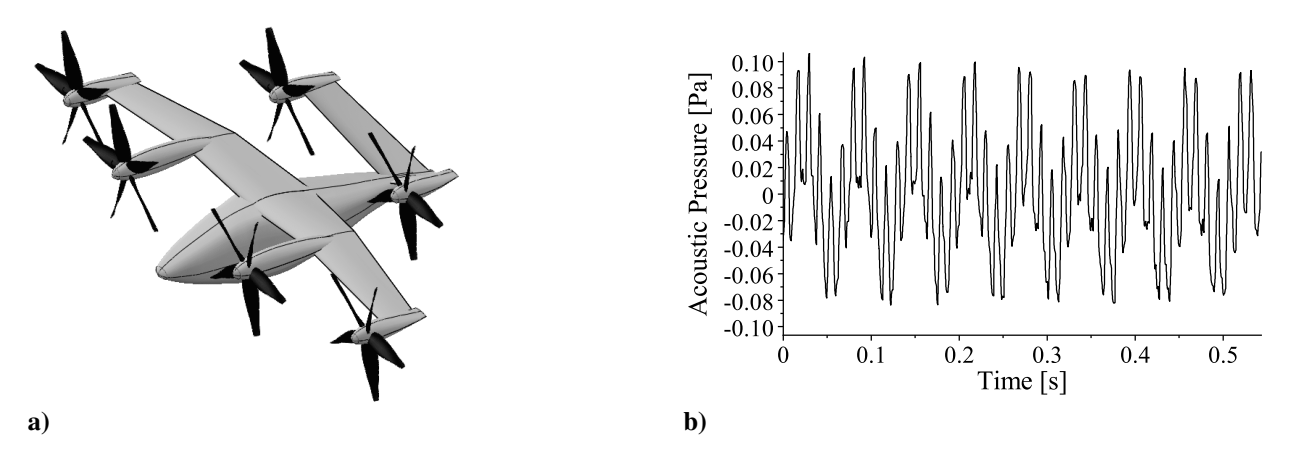


Fig. 11. Sketch of a) aircraft vehicle 2 based on the OpenVSP six-propeller Joby S4 UAM eVTOL concept and b) its pressure-time history recorded at the peak observer angles (70° and 290°) leading to the maximum in-plane OASPL (77.3 dB) at 50 m from the vehicle's centroid.

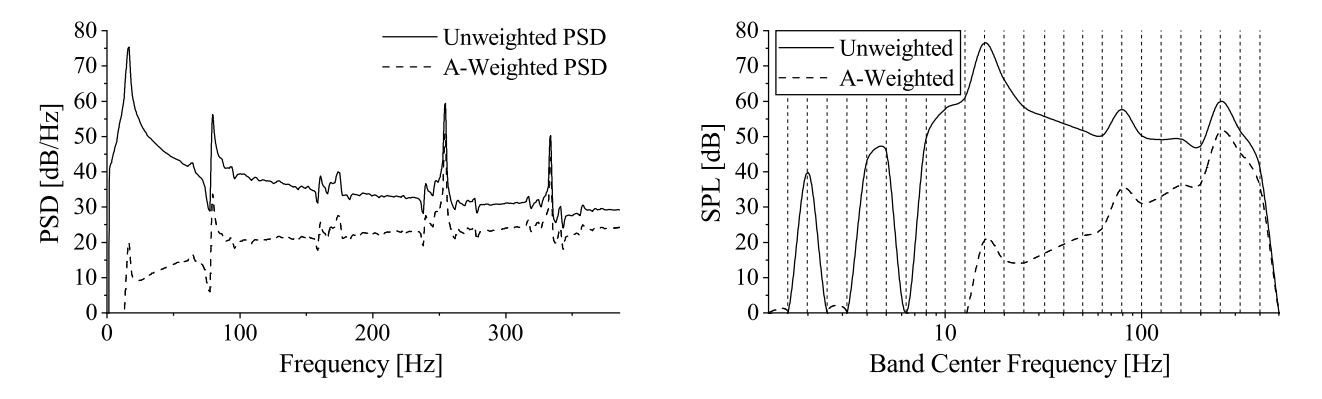


Fig. 12. Vehicle 2 distribution of both unweighted and A-weighted a) PSD and b) PBS measurements.

the propeller's RPM (15.9 Hz), with secondary contributions caused by harmonics associated with the blade passage frequency. In this configuration, as in the first case, spikes along multiples of the blade passage frequency, 15.9 Hz, 79.6 Hz, 159 Hz, 239 Hz, and 318 Hz are detected. The corresponding PBS plots in Fig. 12b confirm that, despite the simultaneous operation of six identical propellers, the largest perceived (A-weighted) contributions to the PBS signal strength correspond to the 1/3-octave band centered at approximately 20.3 Hz, with a close second and third at around 80 Hz and 250 Hz, progressively. Comparing Cases 1 and 2, where the maximum OASPL measurements return 65.6 dB and 77.3 dB, respectively, we may conclude that the simultaneous operation of several propellers and methodical superposition of their collective SPL values clearly lead to stronger signal strength across all frequencies than using a single propeller.

Moreover, and similarly to Case 1, we find that the largest physical contributor to the acoustic signal does not correspond to the largest perceived contributor to the noise signal. The aircraft propeller noise, when heard by humans, is clearly dominated by its higher frequency tones that are more easily sensed by humans. These higher frequency tones are intimately related to the number and size of propellers on the aircraft. For a given design team, the analysis may lead to a decision to reduce or increase the number of propellers in order to mitigate the perceived intensity of higher frequency tones.

In addition to pressure-time, PSD, and PBS computations, OASPL maps are generated and displayed in Fig. 13a for the multi-propeller driven case; these are produced at fixed radii of 50 m, 100 m, and 150 m, respectively. For this case study, the use of multiple radii for generating OASPL maps helps to ascertain the effect of distance on signal strength and the expected attenuation as the distance from the source is increased. As before, the air flow is directed axially from the $180^{\circ}-0^{\circ}$ station into the propeller that faces it. Unsurprisingly, the loudest signal (83 dB) is observed at nearly-right angles to the propeller blades while facing the tips of the blades, specifically at 70° and 290° . However, in contrast to Case 1, the presence of multiple propellers leads to a small spike in Fig. 13a that corresponds to an observer location of 0° , immediately behind the aircraft. The source of this peculiarity may be attributed to both constructive and destructive interferences, which are brought to bear through the use of multiple propellers.

Moreover, and in accordance with the *inverse-square-distance* law for spherical pressure wave strength propagation, we see in Fig. 13a and Fig. 8a a distinct 6 dB loss in signal strength each time the observer radial distance is doubled. This occurs when the radius is increased from 50 m to 100 m; we also incur an additional 3.5 dB loss in signal strength as the distance from the source is increased from 100 m to 150 m. These values help to confirm that the mathematical framework that we have implemented is capable of accurately predicting the power-distance relations for acoustic pressure signals. Furthermore, and in conformity with Case 1, out-of-plane OASPL data is computed and shown in Fig. 13b for measurements taken in three descending horizontal planes of 50 m, 100 m, and 150 m below the aircraft. We note in this regard that as the observer field shifts vertically downwardly away from the aircraft, the angular locations of the minimum and maximum OASPL values appear to be different from those of Case 1 as well as

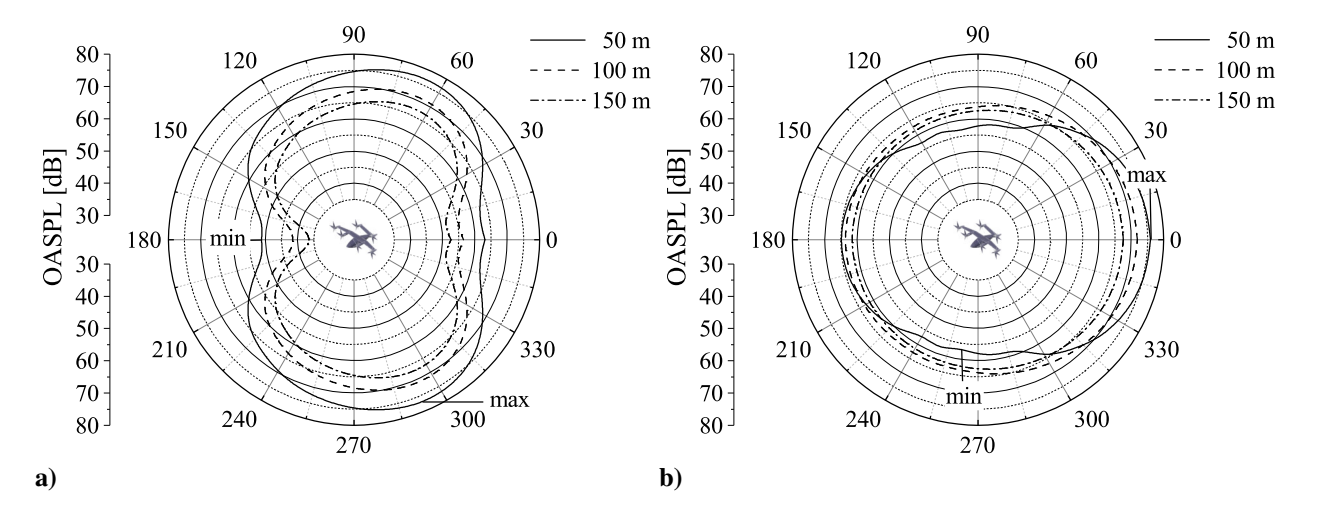


Fig. 13. Vehicle 2 OASPL vs. observer angle for a) three in-plane observers located at 50 m, 100 m, and 150 m horizontal radii around the vehicle's centroid and b) three out-of-plane observers located at a 50 m horizontal radius and situated at a vertical distance of 50 m, 100 m, and 150 m below the aircraft.

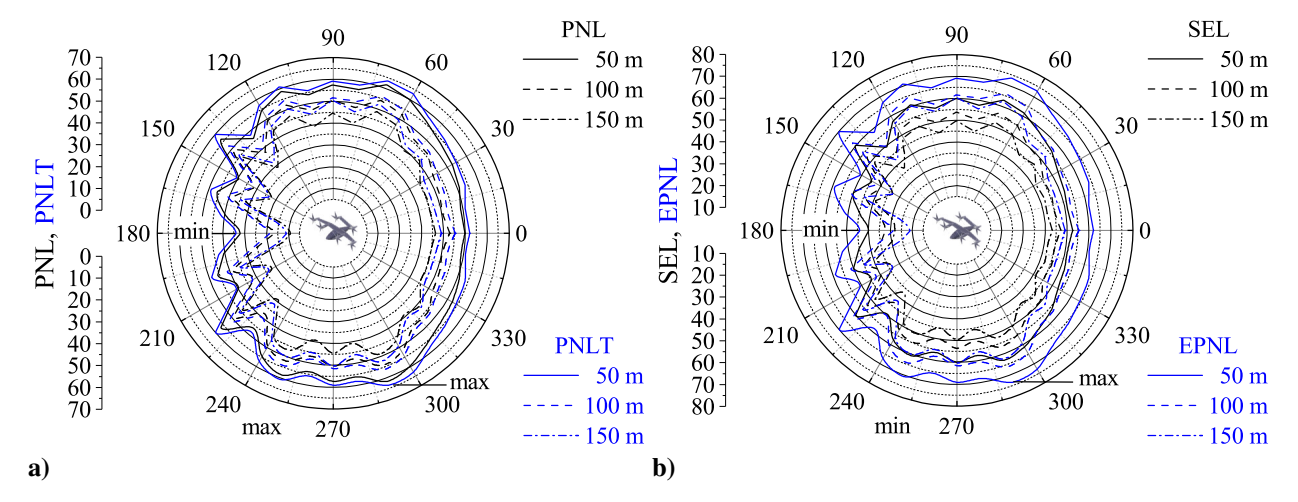


Fig. 14. Vehicle 2 distribution of a) PNL and PNLT as well as b) SEL and EPNL measurements acquired at three in-plane observers located at 50 m, 100 m, and 150 m from the vehicle's centroid.

the in-plane computations of Fig. 13a. Caused mainly by the combined effects of multiple propellers, the maximum OASPL is seen to shift to the 0° location, immediately behind the aircraft. Conversely, the minimum OASPL may be seen to move to around 100° and 260° symmetrically about the 180°-0° line. This is not surprising because increasing the distance below the aircraft makes the distance between the propellers and the vehicle's centroid negligible relative to the overall distance to the 50 m circle of detection. Moreover, as we shift to lower planes of detection, the tendency to approach a rather uniform intensity at a given radius around the vehicle's centroid can be seen. As a result, the shifting of the maximum OASPL to the rear of the aircraft, where sound generated from the various propellers seems to converge, can be observed first at 50 m, and then quite evenly all around the aircraft as the distance reaches 150 m. Similar arguments can be used to explain the redistribution of OASPL intensities along the 90° and 270° stations below the aircraft.

Following the in-plane and out-of-plane contours of OASPL measurements, computations of the corresponding PNL, PNLT, SEL, and EPNL are provided in Fig. 14. Compared to Case 1, it appears that the presence of multiple propellers leads to a markedly different sound structure including signal perception levels all around the vehicle. While the locations associated with the highest and lowest values remain virtually unchanged, it may be seen that the inclusion of pure tonal contributions within the signals can have a considerable impact, especially at observation points in front of the vehicle. In this case, the directionality of the sound at different angles, particularly in front of the vehicle, becomes quite noticeable. This angular dependence is reflected in the sound undulations between 90° and 270°, where an apparent increase in signal strength results in six discrete spikes in each of Fig. 14a and Fig. 14b. Similarly to the results associated with a single propeller, the inclusion of tone-corrections leads to an unmistakable increase in perceived loudness for all observers around the aircraft, including those stationed at the locations of peak intensity. In this case, the maximum values of the calculated PNL, PNLT, SEL, and EPNL are found to be 61.7 PNLdB, 63.4 PNLdB, 62.8 dB, and 73.4 dB, respectively. Due to the inherent symmetry of sound sources with respect to the fuselage, which is aligned with the 180°–0° direction, all peak values are detected evenly at both 70° and 290°.

C. Case 3: Distributed Electric Propulsion (DEP) Vehicle with Multiple Pusher Propellers

The third case study is performed on a pusher-propeller DEP UAM vehicle modeled using NASA's OpenVSP file of the Kittyhawk KH-H1 DEP vehicle. The purpose here is to demonstrate the difference in acoustic signatures from two dissimilar conceptual UAM/DEP designs underlying Cases 2 and 3.

It should be noted that the KH-H1 vehicle exhibits 8 pusher-type propellers in the forward-flight mode as shown in Fig. 15a. In this configuration, the two pairs of inboard wing propellers are operated at 1430 RPM (23.4 Hz) with a slightly reduced tip Mach number of Ma = 0.2. As for the wingtip propellers, they are operated at a higher revolution rate of 1670 RPM (27.8 Hz) with a slightly increased tip Mach number of Ma = 0.25. Lastly, the canard propellers are operated at the highest revolution rate of 1910 RPM (31.8 Hz) with the highest tip Mach number of Ma = 0.28. All

propellers are assumed to remain in phase and the vehicle is operated in forward-flight mode.

As usual, an example pressure-time signal that is representative of the highest acoustic pressure level at a fixed radius of 50 m is provided in Fig. 15b. Furthermore, both weighted and unweighted PSD and PBS distributions are displayed side-by-side in Figs. 16a and 16b. Along with frequency domain metrics, the computed in-plane and out-of-plane OASPL values are further reported on a polar chart in Figs. 17a and 17b. Here too, the flow is directed toward the propeller face axially along the 180°–0° horizontal line. On the one hand, for the in-plane measurements in Fig. 17a, the signal is physically strongest at right angles to the aircraft and propeller blades, specifically at 90° and 270°, where the OASPL reaches a value of 53.0 dB at a radius of 50 m. On the other hand, for the out-of-plane measurements in Fig. 17b, which are collected at 50 m below the aircraft, the maximum OASPL drops to 50.9 dB at 0°. Overall, the reshaping of the OASPL distribution in the out-of-plane measurements seems consistent with the trends characterizing Case 2 in Fig. 13b. In both instances, the OASPL approaches a progressively more uniform distribution around the vehicle with successive increases in the vertical distance from the source.

Despite the emergence of several contributing harmonic tones, one may also anticipate seeing three distinct spikes of equal magnitude, i.e., for each of the three different propeller RPMs being used. These are realized in the three spikes at the left of the PSD plot. Turning our attention to the PBS distribution in Fig. 16b, it is gratifying to see that these three particular tones correspond to the largest physical contribution to the signal intensity, which is reflected in the frequency band that is centered at 23.4 Hz. However, when human perception in the form of an A-weighted PBS distribution is accounted for, it can be seen that the largest human-perceived detection band shifts toward the band centered at 43.2 Hz. Overall, it may be interesting to note the change in the power distribution shape, which is based on the change in aircraft geometry and propeller location. Given the forward swept wings on the aircraft, it becomes



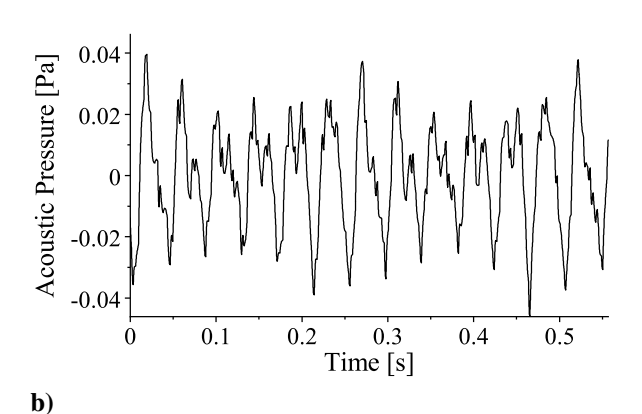
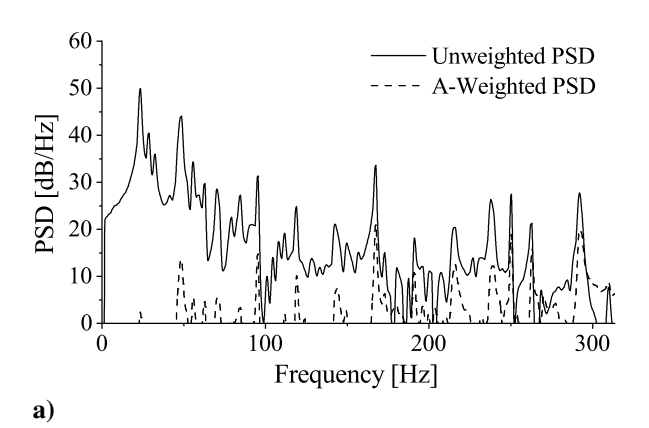


Fig. 15. Sketch of a) aircraft vehicle 3 based on the OpenVSP Kittyhawk KH-H1 DEP concept and b) its pressure-time history recorded at the peak observer angles (90° and 270°) leading to the maximum in-plane OASPL (58.6 dB) at 50 m from the vehicle's centroid.



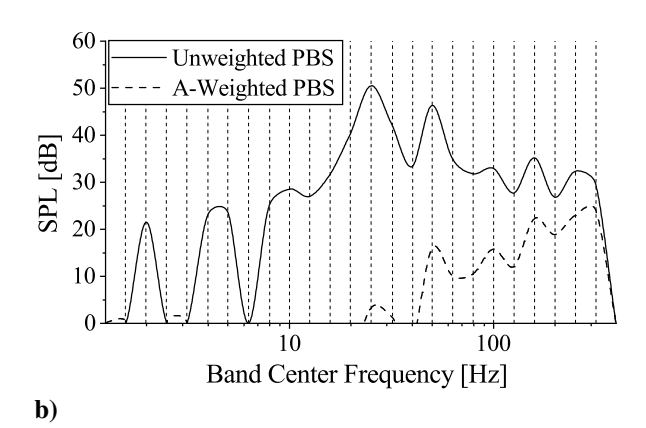


Fig. 16. Vehicle 3 distribution of both unweighted and A-weighted a) PSD and b) PBS measurements.

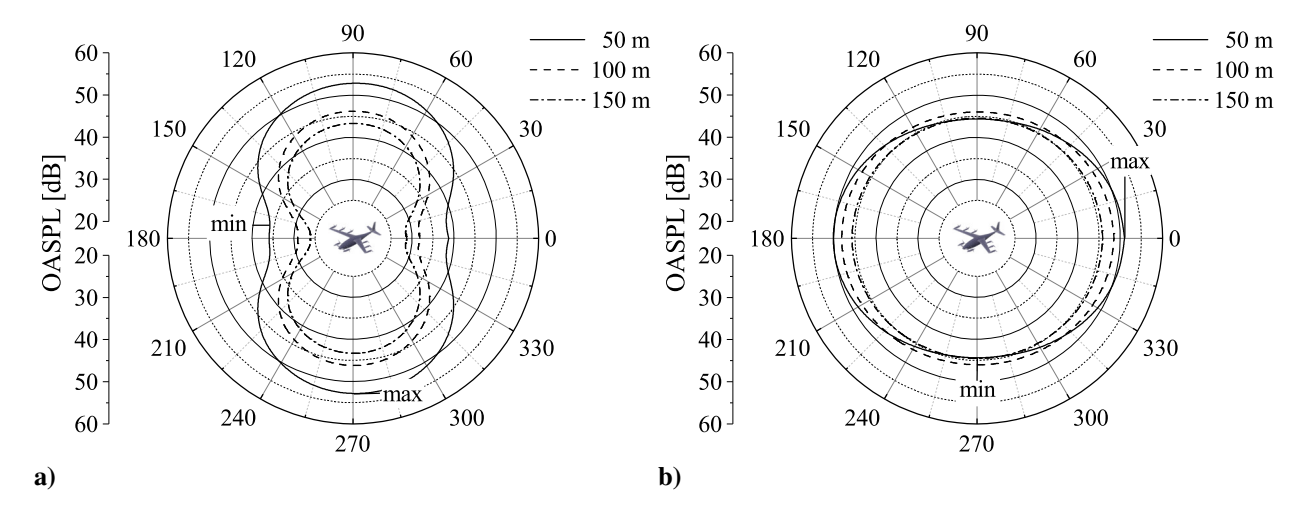


Fig. 17. Vehicle 3 OASPL vs. observer angle for a) three in-plane observers located at 50 m, 100 m, and 150 m horizontal radii around the vehicle's centroid and b) three out-of-plane observers located at a 50 m horizontal radius and situated at a vertical distance of 50 m, 100 m, and 150 m below the aircraft.

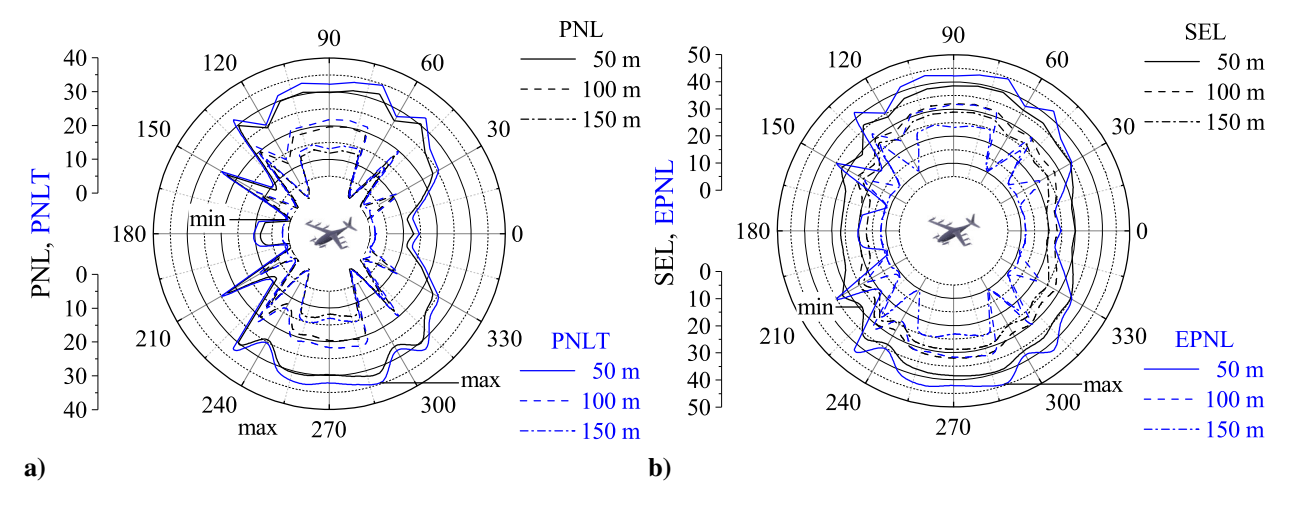


Fig. 18. Vehicle 3 distribution of a) PNL and PNLT as well as b) SEL and EPNL measurements acquired at three in-plane observers located at 50 m, 100 m, and 150 m from the vehicle's centroid.

rather apparent that propeller location and aircraft shape have appreciable effects on the overall distribution of signal power. It is also interesting to note that the distribution of PSD peaks corresponds to the propeller's revolution rate, number of blades, and associated harmonic frequencies.

Lastly, as for the metrics that account for human perception and tonality effects, the relevant characteristics are provided in Fig. 18. In comparison to the OASPL contours, one can observe noticeable deviations in the overall distribution of the perceived intensity of the vehicle's acoustic signal, specifically, in relation to the distribution of raw physical sound intensity in Fig. 17. Similarly to Case 2, the visual representations in Fig. 18 confirm that the perceived loudness of a signal becomes highly angle dependent, judging by the sharp distortions of the contour plots at distinct observer locations. In fact, this heightened spatial sensitivity of the metrics may be attributed to the presence of several additional pure tones stemming from different propeller revolution rates and blade speeds accumulating at different observer locations. Although the angles at which the maximum and minimum values of these metrics remain largely unchanged, the deviations in perceived signal intensities can differ by 5-10 dB based on the observer's angular orientation, notwithstanding the distance from the vehicle. Here too, because of the strict symmetry of the propellers about the fuselage's *X*-axis, the peak values of all four properties are detected equally at both 70° and 290°. As for their peak values, they are found to be 31.7 PNLdB, 34.4 PNLdB, 39.1 dB, and 44.4 dB for the PNL, PNLT, SEL, and EPNL signals, respectively.

D. Tabulated Results

For the reader's convenience, a tabulated list of characteristic metrics associated with the three illustrative cases, including the locations and values of corresponding extrema, are evaluated and cataloged in Table 1. These include four global properties, the SEL, PNL, PNLT, and EPNL, which have been defined in Sec. II, and not yet computed. The resulting side-by-side comparison enables us to identify the common features as well as the dissimilarities among the three cases in question. For example, a direct correlation may be seen to exist between achieving higher peak OASPL values and possessing more propellers or higher tip Mach numbers. This anticipated dependence helps to explain the reason for the largest OASPL_{max} of 77.3 dB being associated with Case 2, and for the lowest OASPL_{max} of 53.0 dB stemming from Case 3. In fact, the same trend may be seen to affect the remaining metrics that include SEL_{max} and EPNL_{max}, with their highest values of 62.8 dB and 73.4 EPNdB corresponding to Case 2 which, unlike Case 3, exhibits the lowest SEL_{max} and EPNL_{max} values of 39.1 dB and 44.4 EPNdB, respectively. One also notes that an aircraft with a symmetric distribution of propellers, such as Cases 2 and 3, gives rise to two symmetric distributions of OASPL_{max}, OASPL_{max}, and SEL_{max}.

Table 1. Summary of characteristic metrics for Cases 1, 2, and 3 for an observer at 50 m from the vehicle

Properties:	Case 1 (Fig. 7a)	Case 2 (Fig. 11a)	Case 3 (Fig. 15a)
Number of propellers	1	6	8
Blades per propeller	5	5	3
Propeller revolution rate	15.9 Hz	15.9 Hz	23.4 Hz, 27.8 Hz, 31.8 Hz
Blade tip Mach number, Ma	0.4	0.4	0.20, 0.25, 0.28
PSD _{max} [dB/Hz] (frequency)	65.4 (16 Hz)	75.4 (16.6 Hz)	49.9 (23.4 Hz)
PSD _{Amax} [dB/Hz] (frequency)	39.4 (254 Hz)	50.9 (255 Hz)	21.1 (168 Hz)
PBS _{max} [dB] (band center frequency)	65.4 (19.5 Hz)	76.4 (20.3 Hz)	50.5 (23.4 Hz)
PBS _{Amax} [dB] (band center frequency)	39.7 (40.9 Hz)	51.3 (42.4 Hz)	24.1 (43.2 Hz)
OASPL _{max} [dB] (observer angle)	65.6 (290°)	77.3 (70°, 290°)	53.0 (90°, 270°)
OASPL _{Amax} [dB] (observer angle)	41.9 (280°)	52.8 (70°, 290°)	29.1 (70°, 290°)
10 s SEL _{max} [dB] (observer angle)	51.9 (280°)	62.8 (70°, 290°)	39.1 (70°, 290°)
PNL _{max} [PNLdB] (observer angle)	47.6 (270°)	61.7 (70°, 290°)	31.7 (70°, 290°)
PNLT _{max} [PNLdB] (observer angle)	49.9 (270°)	63.4 (70°, 290°)	34.4 (70°, 290°)
10 s EPNL _{max} [EPNdB] (observer angle)	59.9 (270°)	73.4 (70°, 290°)	44.4 (70°, 290°)

IV. Conclusion

In this work, a set of seven particularly useful acoustic metrics that are relevant to the analysis of sound pressure levels, power levels, frequency spectra, power distributions, and perceived noisiness produced by an aircraft in flight are identified and defined. It is also shown how the corresponding calculations can be practically implemented in conjunction with a surface-vorticity solver, namely, FlightStream®. In this work, these metrics are evaluated and discussed in the context of several UAM vehicles with dissimilar acoustic signal characteristics. The analysis provided through our designated metrics leads to useful insights into the topological characteristics of a given acoustic signal. These characteristics include the physical and perceived qualities of the noise as well as vital extensions to view spatial distributions of the acoustic power within the observer field over particularly meaningful bandwidths. In this manner, the combination of the aforementioned figures of merit stands to supply the aircraft design teams with an assortment of measures that can facilitate the identification of both actual and perceived aeroacoustic noise levels and locations early in the design phase. It can thus be seen that, with this predictive capability at their disposal, design teams are able to assemble the information necessary to make surgical improvements and precise modifications that enable the aircraft in question to meet FAA and ICAO regulations. Ultimately, with an efficient implementation of these metrics into a fast-performing and reliable flow solver, aeroacoustic analysis can be readily integrated into the early design phases of a developmental program, thus ensuring a seamless transition from a conceptual vehicle design room to a commercial platform.

Acknowledgments

The authors wish to acknowledge the cooperation and support of the NASA researchers and the NASA SBIR Office on this effort. The primary work for this study was performed within the context of the NASA STTR 80NSSC20C0586 Phase I contract activity.

Appendix

A. DFT Matrix

As previously defined, the DFT algorithm takes a collection of "N" points and transforms its components into their Fourier coefficient counterparts, $\{f_0, f_1, f_2, \dots, f_{N-1}\} \rightarrow \{\hat{f_0}, \hat{f_1}, \hat{f_2}, \dots, \hat{f_{N-1}}\}$, where f_n and $\hat{f_n}$ refer to the nth sample data and Fourier coefficients, respectively. This transformation may be accomplished by taking,

$$\hat{f}_n = \sum_{m=0}^{N-1} f_m e^{-2mn\pi i/N}, \tag{24}$$

and, inversely,

$$f_n = \frac{1}{N} \sum_{m=0}^{N-1} \hat{f}_m \ e^{2mn\pi i/N}. \tag{25}$$

The exponential coefficient contained in this expression may be replaced by some complex frequency coefficient, ω_n , where

$$e^{-2n\pi i/N} = \omega_n. (26)$$

Based on this definition, one can compute a "DFT matrix" encapsulating the Fourier transformation, which we will call **F**. The DFT can then be written as $\hat{f} = \mathbf{F} \cdot f$ or, explicitly,

$$\begin{bmatrix} \hat{f}_{0} \\ \hat{f}_{1} \\ \hat{f}_{2} \\ \vdots \\ \hat{f}_{N-1} \end{bmatrix} = \begin{bmatrix} 1 & 1 & 1 & \cdots & 1 \\ 1 & \omega_{1} & \omega_{1}^{2} & \cdots & \omega_{1}^{(N-1)} \\ 1 & \omega_{2}^{1} & \omega_{2}^{2} & \cdots & \omega_{2}^{(N-1)} \\ \vdots & \vdots & \vdots & \ddots & \vdots \\ 1 & \omega_{N-1}^{1} & \omega_{N-1}^{2} & \cdots & \omega_{N-1}^{N-1} \end{bmatrix} \begin{bmatrix} f_{0} \\ f_{1} \\ f_{2} \\ \vdots \\ f_{N-1} \end{bmatrix}.$$

$$(27)$$

In practice, $\mathbf{F} \cdot \mathbf{f}$ can be quite expensive to compute, having a size that is proportional to $O(N^2)$.

B. FFT Algorithm

This is where the Fast Fourier Transform's advantage can be seen. Based on its fundamental definition, the DFT calculation requires $O(N^2)$ calculations, whereas the FFT calculation has an almost *linear* relation between data points and computational cost, specifically, $O(N \log N)$. It should be noted that, at small values of N, the difference between the standard DFT and FFT algorithm remains negligible; however, as N increases beyond approximately 100, the advantage of the FFT can translate into several orders of magnitude in run-time savings.

For example, given a typical 10 s audio signal, which is sampled at 440 kHz, we obtain $N = 4.4 \times 10^5$ data points to manipulate. Comparing the FFT and traditional DFT formulations, the increase in computational efficiency consists of a factor of roughly 100,000 times. The FFT algorithm takes advantage of the extensive symmetry throughout the DFT matrix.

When it was first being studied, the FFT was only applied to specific values of N, specifically, for even values of N. When extending this data set where $N \neq 2^k$, a transform known as the "chirp-z transformation," or "zero-padding" may be applied to the given data set. For convenience, we find it useful to define a special FFT algorithm that is ideally suited for cases with $N = 2^k$.

To illustrate this operation, consider a data set of size N, where $N = 2^{10} = 1024$. The DFT matrix can be factored and the DFT rewritten using:

$$\widehat{f} = \mathbf{F}_{n} \cdot f = \begin{bmatrix} 1 & 1 & 1 & \cdots & 1 \\ 1 & \omega_{1} & \omega_{1}^{2} & \cdots & \omega_{1}^{(N-1)} \\ 1 & \omega_{2}^{1} & \omega_{2}^{2} & \cdots & \omega_{2}^{(N-1)} \\ \vdots & \vdots & \vdots & \ddots & \vdots \\ 1 & \omega_{N-1}^{1} & \omega_{N-1}^{2} & \cdots & \omega_{N-1}^{N-1} \end{bmatrix} \begin{bmatrix} f_{0} \\ f_{1} \\ f_{2} \\ \vdots \\ f_{N-1} \end{bmatrix} = \begin{bmatrix} \mathbb{I} & -\mathbb{D}_{N/2} \\ \mathbb{I} & -\mathbb{D}_{N/2} \end{bmatrix} \begin{bmatrix} \mathbf{F}_{N/2} & 0 \\ 0 & \mathbf{F}_{N/2} \end{bmatrix} \begin{bmatrix} f_{\text{even}} \\ f_{\text{odd}} \end{bmatrix}. (28)$$

In the above, \mathbb{I} represents an identity matrix, \mathbb{D}_N refers to a diagonal matrix of size N, and $\mathbf{F}_{N/2}$ denotes a DFT matrix of size N/2; lastly, \mathbf{f}_{even} and \mathbf{f}_{odd} stand for the even and odd indexed data points of the original data vector \mathbf{f} . It may be instructive to note that the process of converting $\mathbf{F}_N \to \mathbf{F}_{N/2}$ may be carried out until N/k = 2, where k is the number of times the method is employed. As such, two iterations of this process yield:

$$\widehat{f} = \begin{bmatrix} \mathbb{I} & -\mathbb{D}_{N/2} \\ \mathbb{I} & -\mathbb{D}_{N/2} \end{bmatrix} \begin{bmatrix} \mathbf{F}_{N/2} & 0 \\ 0 & \mathbf{F}_{N/2} \end{bmatrix} \begin{bmatrix} f_{\text{even}} \\ f_{\text{odd}} \end{bmatrix},$$
 (29)

$$\widehat{f} = \begin{bmatrix} \mathbb{I} & -\mathbb{D}_{N/2} \\ \mathbb{I} & -\mathbb{D}_{N/2} \end{bmatrix} \begin{bmatrix} \begin{bmatrix} \mathbb{I} & -\mathbb{D}_{N/4} \\ \mathbb{I} & -\mathbb{D}_{N/4} \end{bmatrix} \begin{bmatrix} \mathbf{F}_{N/4} & 0 \\ 0 & \mathbf{F}_{N/4} \end{bmatrix} & 0 \\ 0 & \begin{bmatrix} \mathbb{I} & -\mathbb{D}_{N/4} \\ \mathbb{I} & -\mathbb{D}_{N/4} \end{bmatrix} \begin{bmatrix} \mathbf{F}_{N/4} & 0 \\ 0 & \mathbf{F}_{N/4} \end{bmatrix} \end{bmatrix} \begin{bmatrix} f_{\text{even-even}} \\ f_{\text{even-odd}} \\ f_{\text{odd-even}} \\ f_{\text{odd-even}}$$

For data sets of size $N=2^{10}$, one gets: $\mathbf{F}_{1024} \rightarrow \mathbf{F}_{512} \rightarrow \mathbf{F}_{256} \rightarrow \cdots \rightarrow \mathbf{F}_4 \rightarrow \mathbf{F}_2$. When carried out to completion, this action specifically reduces the computational cost by almost a whole factor of N. In standard notation, this transformation can be expressed as:

$$\hat{f}_{n} = \sum_{m=0}^{N-1} f_{m} e^{-i\frac{2\pi mn}{N}} = \sum_{m=0}^{N/2-1} f_{2m} e^{-i\frac{2\pi n}{N}(2m)} + \sum_{m=0}^{N/2-1} f_{2m+1} e^{-i\frac{2\pi n}{N}(2m+1)}$$

$$= \sum_{m=0}^{N/2-1} f_{2m} e^{-i\frac{2\pi n}{N}(2m)} + \left(e^{-i\frac{2\pi n}{N}}\right) \sum_{m=0}^{N/2-1} f_{2m+1} e^{-i\frac{2\pi n}{N}(2m)} = E_{n} + e^{-i\frac{2\pi n}{N}} O_{n}.$$
(31)

Variations of this method can be found in the literature, some of which include using factors 4 and 8 instead of 2 [52].

References

- [1] Asimov, I., Asimov's Biographical Encyclopedia of Science and Technology, Doubleday, 1982.
- [2] Vitruvius, M., The Ten Books on Architecture, Harvard University Press, 1914.

- [3] Boethius, A. M. S., Fundamentals of Music, Yale University Press, 1989.
- [4] Marsenne, M., Harmonie Universelle Contenant la Theorie et la Pratique de la Musique, Springer Netherlands, 1957.
- [5] Dostrovsky, S., Campbell, M., Bell, J., and Truesdell, C., Physics of Music, 2001.
- [6] Lenihan, J., "Mersenne and Gassendi," Acta Acustica united with Acustica, Vol. 1, No. 2, 1951, pp. 96–99.
- [7] Lenihan, J. M. A., "The Velocity of Sound in Air," Acustica, Vol. 2, No. 5, 1952, pp. 205–212.
- [8] Lindsay, R. B., "The Story of Acoustics," The Journal of the Acoustical Society of America, Vol. 39, No. 4, 1966, pp. 629–644. doi:10.1121/1.1909936.
- [9] D'Alembert, J., "Researches on the Curve that a Tense Cord Forms when Set Into Vibration," Histoire de l'Academie Royale Des Sciences et Belles Lettres de Berlin, 1747.
- [10] Helmholtz, H. L. F., On the Sensations of Tone as a Physiological Basis for the Theory of Music, Cambridge University Press, 1875.
- [11] Gauss, C. F., "Theoria Interpolationis Methodo Nova Tractata (Theory Regarding a New Method of Interpolation)," Werke, Königlichen Gesellschaft der Wissenschaften zu Göttingen, Vol. 3, 1866, pp. 265–303. doi:10.1007/978-3-642-49319-5_8.
- [12] Cooley, J. W. and Tukey, J. W., "An Algorithm for the Machine Calculation of Complex Fourier Series," *Mathematics of Computation*, Vol. 19, No. 90, 1965, pp. 297–301. doi:10.2307/2003354.
- [13] Strutt, J. W., The Theory of Sound, Vol. 2, Macmillan, 1896.
- [14] Stokes, G. G., "On the Theories of the Internal Friction of Fluids in Motion, and of the Equilibrium and Motion of Elastic Solids," 1880, pp. 75–129. doi:10.1017/cbo9780511702242.005.
- [15] Lighthill, M. J., "On Sound Generated Aerodynamically I. General Theory," *Proceedings of the Royal Society. Series A. Mathematical, Physical and Engineering Sciences*, Vol. 211, No. 1107, March 1952, pp. 564–587. doi:10.1098/rspa.1952.0060.
- [16] Lighthill, M. J., "On Sound Generated Aerodynamically II. Turbulence as a Source of Sound," Proceedings of the Royal Society of London. Series A. Mathematical and Physical Sciences, Vol. 222, No. 1148, 1954, pp. 1–32. doi:10.1098/rspa.1954.0049.
- [17] Curle, N., "The Influence of Solid Boundaries Upon Aerodynamic Sound," Proceedings of the Royal Society of London. Series A. Mathematical and Physical Sciences, Vol. 231, No. 1187, 1955, pp. 505–514. doi:10.1098/rspa.1955.0191.
- [18] Ffowcs Williams, J. E., "The Noise From Turbulence Convected at High Speed," *Philosophical Transactions of the Royal Society of London. Series A, Mathematical and Physical Sciences*, Vol. 255, No. 1061, 1963, pp. 469–503. doi:10.1098/rsta.1963.0010.
- [19] Lowson, M. V., "The Sound Field for Singularities in Motion," Proceedings of the Royal Society of London. Series A. Mathematical and Physical Sciences, Vol. 286, No. 1407, 1965, pp. 559–572. doi:10.1098/rspa.1965.0164.
- [20] Ffowcs Williams, J. E. and Hawkings, D., "Sound Generation by Turbulence and Surfaces in Arbitrary Motion," *Philosophical Transactions of the Royal Society of London. Series A, Mathematical and Physical Sciences*, Vol. 264, No. 1151, 1969, pp. 321–342. doi:10.1098/rsta.1969.0031.
- [21] Farassat, F., "Theory of Noise Generation from Moving Bodies with an Application to Helicopter Rotors," Technical Report NASA Technical Report No. TR R-451, National Aeronautics and Space Administration, NASA Langley Research Center, Hampton, VA, 1975.
- [22] Farassat, F. and Succi, G. P., "A Review of Propeller Discrete Frequency Noise Prediction Technology with Emphasis on Two Current Methods for Time Domain Calculations," *Journal of Sound and Vibration*, Vol. 71, No. 3, August 1980, pp. 399–419. doi:10.1016/0022-460x(80)90422-8.
- [23] Brentner, K., "Prediction of Helicopter Rotor Discrete Frequency Noise," Technical Report NASA Technical Memorandum No. TM-87721, National Aeronautics and Space Administration, NASA Langley Research Center, Hampton, VA, 1986.
- [24] Farassat, F., Padula, L., and Dunn, M. H., "Advanced Turboprop Noise Prediction Based on Recent Theoretical Results," *Journal of Sound and Vibration*, Vol. 119, No. 1, November 1987, pp. 53–79. doi:10.1016/0022-460X(87)90189-1.

- [25] Lopes, L. and Burley, C., "Design of the Next Generation Aircraft Noise Prediction Program: ANOPP2," 17th AIAA/CEAS Aeroacoustics Conference (32nd AIAA Aeroacoustics Conference), AIAA Paper No. 2011-2854, Portland, Oregon, June 2011. doi:10.2514/6.2011-2854.
- [26] Dunn, M. H. and Tarkenton, G. M., "Computational Methods in the Prediction of Advanced Subsonic and Supersonic Propeller Induced Noise: ASSPIN Users' Manual," Technical Report NASA Contractor Report No. CR-4434, National Aeronautics and Space Administration, NASA Langley Research Center, Hampton, VA, 1992.
- [27] Shirey, J., Brentner, K., and Chen, H.-n., "A Validation Study of the PSU-WOPWOP Rotor Noise Prediction Code," 45th AIAA Aerospace Sciences Meeting and Exhibit, AIAA Paper No. 2007-1240, Reno, Nevada, January 2007. doi:10.2514/6.2007-1240.
- [28] McKay, R. and Kingan, M. J., "Multirotor Unmanned Aerial System Propeller Noise Caused by Unsteady Blade Motion," 2019 AIAA/CEAS Aeroacoustics Conference, AIAA Paper 2019-2499, May 2019. doi:10.2514/6.2019-2499.
- [29] Jia, Z. and Lee, S., "Acoustic Analysis of a Quadrotor eVTOL Design Via High-fidelity Simulations," 2019 AIAA/CEAS Aeroacoustics Conference, AIAA Paper 2019-2631, May 2019. doi:10.2514/6.2019-2631.
- [30] Lee, H. and Lee, D.-J., "Rotor Interactional Effects on Aerodynamic and Noise Characteristics of a Small Multirotor Unmanned Aerial Vehicle," *Physics of Fluids*, Vol. 32, No. 4, April 2020, pp. 047107. doi:10.1063/5.0003992.
- [31] Gwak, D. Y., Han, D., and Lee, S., "Sound Quality Factors Influencing Annoyance from Hovering UAV," *Journal of Sound and Vibration*, Vol. 489, December 2020, pp. 115651. doi:10.1016/j.jsv.2020.115651.
- [32] Smith, D. A., Filippone, A., and Bojdo, N., "Noise Reduction of a Counter Rotating Open Rotor through a Locked Blade Row," *Aerospace Science and Technology*, Vol. 98, March 2020, pp. 105637. doi:10.1016/j.ast.2019.105637.
- [33] Krishnamurthy, S., Rizzi, S. A., Cheng, R., Boyd, D. D., and Christian, A. W., "Prediction-based Auralization of a Multirotor Urban Air Mobility Vehicle," 2021 AIAA SciTech Forum, AIAA Paper 2021-0587, January 2021. doi:10.2514/6.2021-0587.
- [34] Jeong, J., Ko, J., Cho, H., and Lee, S., "Random Process-based Stochastic Analysis of Multirotor Hovering Noise Under Rotational Speed Fluctuations," *Physics of Fluids*, Vol. 33, No. 12, December 2021, pp. 127107. doi:10.1063/5.0071850.
- [35] Dbouk, T. and Drikakis, D., "Quadcopter Drones Swarm Aeroacoustics," Physics of Fluids, Vol. 33, No. 5, May 2021, pp. 057112. doi:10.1063/5.0052505.
- [36] Fenyvesi, B., Kriegseis, J., and Horváth, C., "An Automated Method for the Identification of Interaction Tone Noise Sources on the Beamforming Maps of Counter-rotating Rotors," *Physics of Fluids*, Vol. 34, No. 4, April 2022, pp. 047105. doi:10.1063/5.0083634.
- [37] Ko, J., Jeong, J., Cho, H., and Lee, S., "Real-Time Prediction Framework for Frequency-Modulated Multirotor Noise," *Physics of Fluids*, Vol. 34, No. 2, February 2022, pp. 027103. doi:10.1063/5.0081103.
- [38] Yucel, S. B., Sahin, M., and Unal, M. F., "Propulsive Performance of Plunging Airfoils in Biplane Configuration," *Physics of Fluids*, Vol. 34, No. 3, March 2022, pp. 033611. doi:10.1063/5.0083040.
- [39] National Bureau of Standards, Standards Yearbook 1931, National Institute of Standards and Technology (NIST), 1931.
- [40] von Békésy, G., "Travelling Waves as Frequency Analysers in the Cochlea," Nature, Vol. 225, No. 5239, 1970, pp. 1207–1209. doi:10.1038/2251207a0.
- [41] Rhode, W. S. and Robles, L., "Evidence from Mössbauer Experiments for Nonlinear Vibration in the Cochlea," *The Journal of the Acoustical Society of America*, Vol. 55, No. 3, 1974, pp. 588–596. doi:10.1121/1.1914569.
- [42] Fletcher, H. and Munson, W. A., "Loudness, Its Definition, Measurement and Calculation," *Journal of the Acoustical Society of America*, Vol. 5, No. 2, October 1933, pp. 82–108. doi:10.1121/1.1915637.
- [43] Wu, J.-Z., Ma, H.-Y., and Zhou, M.-D., Vorticity and Vortex Dynamics, Springer, Berlin, May 2006.
- [44] Ahuja, V., Burkhalter, J., and Hartfield, R. J., "Robust Prediction of High Lift Using Surface Vorticity Phase II Final Report," Technical Report NASA SBIR Report No. NNX17CL12C, Research in Flight Company, LLC, Opelika, AL, 2017.
- [45] Ahuja, V., Burkhalter, J., and Hartfield, R. J., "Early-Design Aeroacoustics Prediction for Distributed Electric Propulsion Vehicles Using FlightStream® Phase I Final Report," Technical Report NASA STTR Report No. 80NSSC20C0586, Research in Flight Company, LLC, Auburn, AL, 2020.

- [46] Ahuja, V. and Hartfield, R. J., "Aerodynamic Loads over Arbitrary Bodies by Method of Integrated Circulation," *Journal of Aircraft*, Vol. 53, No. 6, November 2016, pp. 1719–1730. doi:10.2514/1.c033619.
- [47] Faure, T. M. and Leogrande, C., "High Angle-of-attack Aerodynamics of a Straight Wing with Finite Span Using a Discrete Vortex Method," *Physics of Fluids*, Vol. 32, No. 10, October 2020, pp. 104109. doi:10.1063/5.0025327.
- [48] Faure, T. M., Roncin, K., Viaud, B., Simonet, T., and Daridon, L., "Flapping Wing Propulsion: Comparison Between Discrete Vortex Method and Other Models," *Physics of Fluids*, Vol. 34, No. 3, March 2022, pp. 034108. doi:10.1063/5.0083158.
- [49] Olson, E. D. and Albertson, C. W., "Aircraft High-Lift Aerodynamic Analysis Using a Surface-Vorticity Solver," 54th AIAA Aerospace Sciences Meeting, AIAA Paper No. 2016-0779, San Diego, California, January 2016. doi:10.2514/6.2016-0779.
- [50] Sandoz, B., Ahuja, V., and Hartfield, R. J., "Longitudinal Aerodynamic Characteristics of a V/STOL Tilt-wing Four-Propeller Transport Model Using a Surface Vorticity Flow Solver," 2018 AIAA Aerospace Sciences Meeting, AIAA Paper No. 2018-2070, Kissimmee, Florida, January 2018. doi:10.2514/6.2018-2070.
- [51] DiMaggio, G. A., Hartfield, R. J., Majdalani, J., and Ahuja, V., "Solid Rocket Motor Internal Ballistics Using an Enhanced Surface-Vorticity Panel Technique," *Physics of Fluids*, Vol. 33, No. 10, October 2021, pp. 103613–16. doi:10.1063/5.0069075.
- [52] Barnett, V. D. and Hamming, R. W., "Numerical Methods for Scientists and Engineers," *Journal of the Royal Statistical Society. Series A*, Vol. 125, No. 4, 1962, pp. 642–643. doi:10.2307/2982636.